AN ABSTRACT OF THE THESIS OF

Fu-lung Chang for the degree of Master of Science in

Atmospheric Sciences presented on July 1, 1991.

Title : Toward the Estimation of Errors in Cloud Cover Derived by Threshold Methods

Redacted for privacy

Abstract approved : _____

James A. Coakley, Jr.

The accurate determination of cloud cover amount is important for characterizing the role of cloud feedbacks in the climate system. Clouds have a large influence on the climate system through their effect on the earth's radiation budget. As indicated by the NASA Earth Radiation Budget Experiment (ERBE), the change in the earth's radiation budget brought about by clouds is $\sim$–15 Wm^{-2} on a global scale, which is several times the $\sim$4 Wm^{-2} gain in energy to the troposphere-surface system that would arise from a doubling of CO_2 in the atmosphere. Consequently, even a small change in global cloud amount may lead to a major change in the climate system.

Threshold methods are commonly used to derive cloud properties from satellite imagery data. Here, in order to quantify errors due to thresholds, cloud cover is obtained using three different values of thresholds. The three thresholds are applied to the 11 μm, $(4\ km)^2$ NOAA-9 AVHRR GAC satellite imagery data over four oceanic regions. Regional cloud-cover fractions are obtained for two different scales, $(60\ km)^2$ and $(250\ km)^2$. The spatial coherence method for obtaining cloud cover from imagery data is applied to coincident data. The differences between cloud cover derived by the spatial coherence method and by the threshold methods depends on the setting of the

threshold. Because the spatial coherence method is believed to provide good estimates of cloud cover for opaque, single-layered cloud systems, this study is limited to such systems, and the differences in derived cloud cover are interpreted as errors due to the application of thresholds. The threshold errors are caused by pixels that are partially covered by clouds and the errors have a dependence on the regional scale cloud cover. The errors can be derived from the distribution of pixel-scale cloud cover.

Two simple models which assume idealized distributions for pixel-scale cloud cover are constructed and used to estimate the threshold errors. The results show that these models, though simple, perform rather well in estimating the differences between cloud cover derived by the spatial coherence method and those obtained by threshold methods.

Toward the Estimation of Errors in Cloud Cover Derived by Threshold Methods

by

Fu-lung Chang

A THESIS

submitted to

Oregon State University

in partial fulfillment of
the requirements for the
degree of

Master of Science

Completed July 1, 1991

Commencement June 1992

APPROVED :

Redacted for privacy

Professor of Atmospheric Sciences in charge of major

Redacted for privacy

Head of Department of Atmospheric Sciences

Redacted for privacy

Dean of Graduate School

Date thesis is presented July 1, 1991

Thesis typed by Fu-lung Chang

ACKNOWLEDGEMENT

I would like to thank my major professor, Dr. James A. Coakley, for his generous guidance, support, and encouragement. His native intellectual abililty and prominent achievement in this field made an invaluable academic experience for me in my research career.

I also thank David V. Judge for his help in computer programming and constant discussions and Andrew S. Kowalski for his valuable comments on an earlier draft.

Special thanks go to my girlfriend, Fangchen Lin, for her taking care of me and sustained encouragement.

This work was supported by the National Science Foundation through Grant ATM-8912669. The NASA ERBE project is also acknowledged for making available the V–5 Scene Identification Validation Data used in this study.

TABLE OF CONTENTS

LIST OF FIGURES

LIST OF TABLES

Toward the Estimation of Errors in Cloud Cover Derived by Threshold Methods

1. Introduction

Clouds have a large influence on the climate. Clouds affect the climate system through their effect on the earth's radiation budget. According to observations from the Earth Radiation Budget Experiment (ERBE), approximately 70–85% (70–85 Wm^{-2} out of 102 Wm^{-2}) of the total sunlight reflected by the earth-atmosphere system is reflected by clouds, and approximately 30–65% (75–154 Wm^{-2} out of 234 Wm^{-2}) of the total radiation emitted by the earth-atmosphere system is emitted by clouds. These numbers indicate that clouds reduce the absorption of incident solar radiation more effectively than they reduce the earth's thermal emission to space. The loss in the earth's radiation budget brought about by the presence of clouds is approximately 15 Wm^{-2} on a global scale (Ramanathan et al., 1989), which is several times the approximately 4 Wm^{-2} gain in energy to the troposphere-surface system due to a doubling of CO_2 in the atmosphere (Ramanathan and Coakley, 1979). Clearly, even a small change in global cloud amount may lead to a major change in the climate.

While attention has been focused on the role of cloud feedbacks on the global-scale climate, how cloud cover actually varies and how such changes might influence the climate are still highly uncertain due to the lack of physically-based global observations of clouds. Reliable observations of cloud cover in space and time are necessary in order to learn more about clouds and to determine quantitatively the contribution of cloud feedback processes to the earth's radiation budget and climate.

Meteorological satellites provide a platform from which to observe clouds over large parts of the earth. Satellite pictures of cloud cover are known all over the world. They have been the most often-used products derived from meteorological satellite imagery data. Satellites measure radiances that are either emitted or reflected

by the earth-atmosphere system. The complexity of the distribution and multi-scale variations of clouds and their interaction with the radiation coming from the sun as well as emitted by the earth's surface and atmosphere make the determination of cloud properties very difficult. Numerous studies have focused on characterizing cloud radiative properties from satellite infrared and/or visible observations. Among these studies, the application of thresholds remains the simplest and the most popular means for determining cloud cover fraction and deducing cloud radiative properties from satellite imagery data (Minnis and Harrison, 1984; Rossow et al., 1984; Rossow et al., 1989).

Since the early 1980's, the International Satellite Cloud Climatology Project (ISCCP) has been using a threshold method to obtain cloud cover. The ISCCP was established as part of the World Climate Research Program (WCRP) in order to gain the needed observations of clouds and to stimulate work towards improving the treatment of clouds in global circulation climate models (Schiffer and Rossow, 1983). However, threshold methods often produce large errors in cloud amount when the coverage in the satellite instrument's field of view or picture element (known as a pixel) is partial. Furthermore, these errors may accumulate to produce large errors in the fractional cloud cover for regions containing many pixels (Shenk and Salomonson, 1972). As a consequence, cloud-cover amount derived by threshold methods like that used by ISCCP is probably biased. The degree of bias needs to be documented (Coakley and Kobayashi, 1989; Coakley, 1991). Here errors in fractional cloud cover obtained with threshold methods are studied and a method for estimating these errors is developed.

In order to assess the errors associated with threshold methods, cloud cover derived by the threshold method is compared with an acceptable reference or "cloud truth" value. However, the determination of what constitutes a reliable "cloud truth" is very difficult. In this study, the spatial coherence method (Coakley and Bretherton, 1982) is used as the source of "cloud truth" data for comparisons.

In 1982, Coakley and Bretherton developed the spatial coherence method for

deriving cloud-cover fraction from high-resolution infrared satellite imagery data. The method takes advantage of a feature common to many large-scale cloud systems, namely, clouds often reside in distinct, well-defined layers and each layer has a temperature commensurate with its altitude. Furthermore, many layered cloud systems are opaque at infrared wavelengths. The method allows for clouds which only partially fill the satellite instrument's field of view. By using the spatial variability of the infrared radiance field, one can identify radiances associated with fields of view that are either completely cloud-free or completely covered by clouds in one or more distinct layers. Because of the layered structure of clouds and because of the opacity of clouds in the 11μm window channel, the spatial coherence method avoids reliance on plane-parallel radiative transfer theory which is thought to be unrealistic for actual clouds (Wielicki and Welch, 1986). As the method uses only the infrared radiance field, it should provide equally good estimates of clear sky and cloudy sky radiances for both daytime and nighttime observations. In addition, for single-layered systems, the cloud cover fraction for a given region may be obtained from the clear sky radiance, the completely cloud-covered radiance, and the mean radiance of the region.

Another objective of this study is to support the goals of ISCCP and the First ISCCP Regional Experiment (FIRE) in order to obtain relevant observations of global-scale cloud systems and to develop empirical estimates of the reliability of cloud properties derived from routine meteorological satellite observations. Comparisons are, therefore, performed by applying both the spatial coherence and threshold methods to coincident (4 km)^2 NOAA-9 Advanced Very High Resolution Radiometer (AVHRR) data with the goal of estimating the probable accuracies of cloud cover derived from satellite imagery data.

Three different thresholds are used in this study to derive fractional cloud cover. The cloud-cover fractions obtained by these threshold methods are compared to those derived by the spatial coherence method. Based on the differences found between the threshold and spatial coherence results, two simple models for estimating errors

in cloud-cover fraction derived by threshold methods are also presented. The results of the comparisons show that the simple models predict rather well the differences between the cloud-cover amount obtained by the spatial coherence method and that derived by the threshold method.

2. Threshold Methods

Most cloud analysis algorithms, such as threshold methods, consist of two basic steps: 1) cloud detection and 2) cloud amount determination. The first step partitions the observed radiances into those representing clear scenes and those representing cloudy scenes. Different algorithms are usually distinguished by how they make this partition. The second step involves the quantitative determination of cloud properties from the measured radiances. This step may be as simple as counting cloudy image pixels to obtain a single parameter like fractional cloud cover or as complex as using radiative transfer models to obtain several parameters. Underlying both of these basic steps is a radiative transfer model. That is, each algorithm is built on the assumption that the atmosphere, surface, and cloud affect the satellite measurement in some specified ways.

The simplest form of the threshold method classifies all image (infrared or visible) pixels as clear or cloudy according to whether the measured radiance (emitted infrared radiances, I, or reflected visible radiances, R) differs from a clear sky value (I_s or R_s) by more than some predetermined threshold amount (ΔI or ΔR). For infrared radiances a pixel is called cloudy if $I < I_s - \Delta I$ (or $R > R_s + \Delta R$ for visible radiances). For the purpose of defining fractional cloud cover, all cloudy pixels are assumed to be 100% cloud covered while clear pixels are assumed to be totally cloud free. The cloud-cover fraction is then given by the ratio of the number of cloudy pixels to the number of total pixels. The mean radiance of clear pixels or cloudy pixels can also be taken to represent some cloud property, namely, I_s=average[I(clear)] and I_c=average[I(cloudy)] (R_s=average[R(clear)] and R_c=average[R(cloudy)]). Such simplicity greatly facilitates the processing of the enormous volumes of data produced by the satellite imagers and thus the threshold technique remains the most popular method for determining cloud properties.

Nevertheless, the assumption that image pixels represent either completely

cloud-covered or completely cloud-free regions is contrary to the observation that often clouds neither completely fill nor completely avoid a satellite instrument's field of view. Most meteorological satellite data are operationally processed with infrared or visible channel resolutions between 1 and 8 km while many cloud elements are smaller than 2 km (Wielicke and Welch, 1986). According to the study of Shenk and Salomonson (1972) a satellite resolution of 0.2 km would be necessary to obtain reasonably accurate fractional cloud cover using a threshold method if cloud elements were 2 km or larger. Even so, pixels on cloud boundaries would still be partially filled. Through theoretical studies and analyses of photographs taken during the Apollo missions, they showed that cloud cover obtained using threshold methods could be overestimated by tens of percent unless the typical cloud sizes were 2 to 3 orders of magnitude larger than the satellite instrument's field of view.

Coakley and Bretherton (1982) plotted the errors obtained by Shenk and Salomonson (1972) against the inverse square root of the cloud-size area to scan-spot-size area ratio. They also indicated that the errors in cloud cover diminish inversely as the square root of the cloud-size area, i.e., as the perimeter of the cloud. This relationship between the error in cloud cover area and the perimeter of the cloud explains why errors obtained with the threshold method are likely to be large unless the clouds are typically much larger than the instrument's field of view. In addition to the dependence on the cloud-areal size distribution, the error in fractional cloud cover derived by a threshold method also depends on the radiative properties of the clouds, the cloud-free background, the setting of the threshold, and the spatial resolution of the satellite instrument.

3. Spatial Coherence Method and Identification of Layered Cloud Systems

The spatial coherence method is applicable to layered cloud systems that extend over moderately large regions $\sim\geq$ (250 km)^2 and which include both completely clear and completely cloud-covered portions that span several fields of view somewhere within the region. Such cloud systems, for example, low-level stratocumulus, appear to be rather common (Brost et al., 1982; Slingo et al., 1982). The method utilizes the local spatial structure of the infrared radiance field to determine the radiances associated with cloud-free and completely cloud-covered fields of view and then to infer the radiances associated with partially-filled fields of view. That is, for single-layered systems radiances of partially covered fields of view are intermediate between the cloud-free and completely cloud-covered radiances.

Figure 3.1(a) shows a spatial coherence arch that is typical of single-layered, low-level systems over oceans. The data is for an area of approximately (250 km)^2 centered at 33.1°S and 85.0°W off the South American coast during the nighttime orbital pass of NOAA–9 on 9 April 1985. The observations are obtained from NOAA-9 AVHRR global area coverage (GAC) data. Each point in the diagram gives the mean and standard deviation of the 11μm radiances for a 2×2 (scan line × scan spot) array of 4 adjacent (4 km)^2 GAC pixels and thus represents an (8 km)^2 portion of the (250 km)^2 frame. There are 1024 points in the arch. The points in the feet of the arch represent portions of the (250 km)^2 frame for which the emission is spatially uniform, at least on the (8 km)^2 scale. To be locally uniform, the emission must be nearly the same for all 4 GAC pixels in the array. Such uniformity is certainly expected for regions over the ocean that are cloud-free and also for regions that are completely covered by clouds which have practically the same heights. Thus, the points in the body of the arch exhibiting locally non-uniform emission are interpreted as partially cloud-covered (8 km)^2 portions of the frame where a layered cloud system breaks

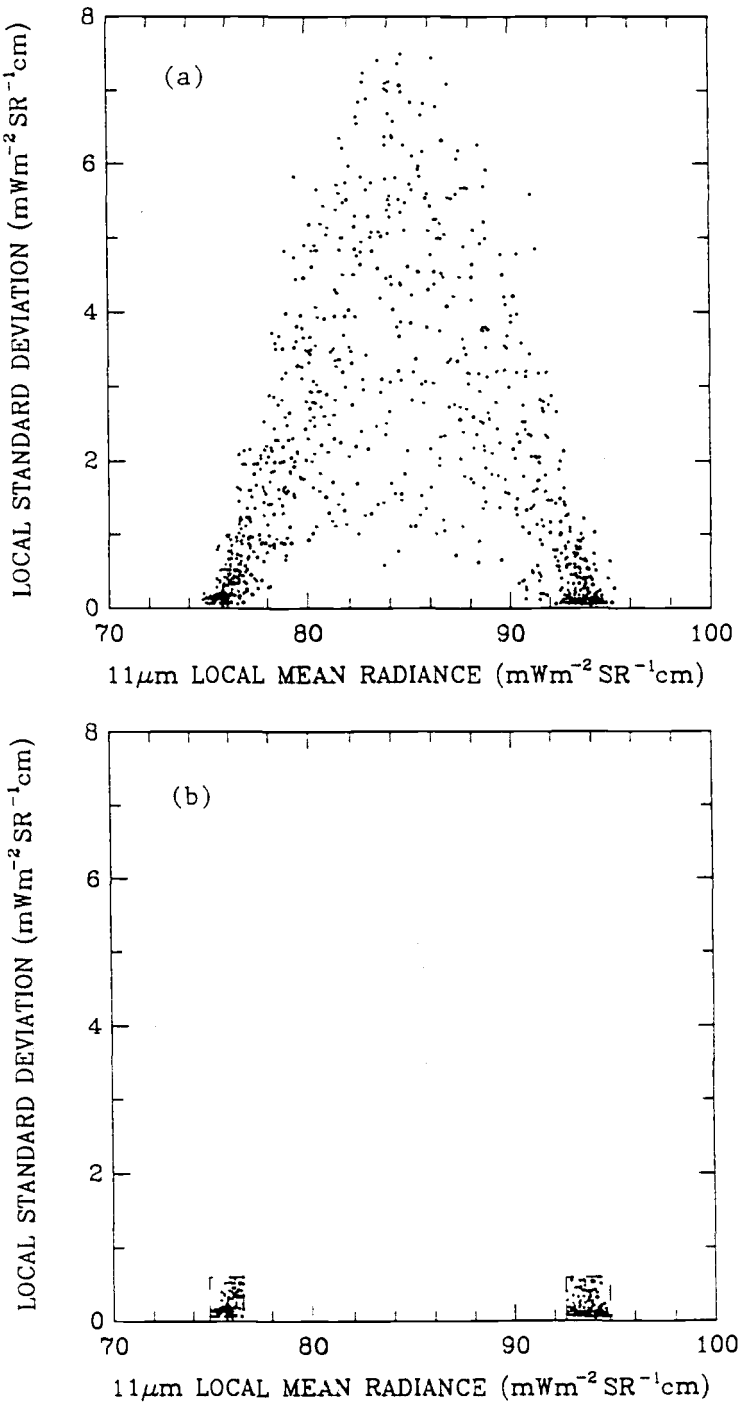

Figure 3.1 (a) Local mean 11μm radiances and local standard deviations for a (250 km)^2 region of the Pacific Ocean at night. Each point gives the mean radiance and standard deviation for the 4 pixels in a 2×2 (scan spot × scan line) array of NOAA-9 AVHRR GAC data. Each point represents an (8 km)^2 portion of the (250 km)^2 region. (b) Points automatically identified as being cloud-free and completely overcast, as described by Coakley and Bretherton (1982).

into cloud elements that are smaller than the AVHRR GAC (4 km)^2 field of view. The cluster of low-variance points in the foot of the arch with high 11μm radiance near 94 mWm^{-2}sr^{-1}cm is interpreted as representing the radiance of cloud-free fields of view, which in this case are clear columns over ocean. The cluster of low-variance points in the foot of the arch with low 11μm radiance near 76 mWm^{-2}sr^{-1}cm is interpreted as representing the radiance of completely cloud-covered fields of view.

When only one layer is evident, as is the case shown in Figure 3.1(a), the fractional cloud cover for the (250 km)^2 region is obtained by assuming that all the clouds in the region belong to a single layer. It is also assumed that the radiance in each pixel consists of the radiance from the cloud-free portion of the pixel and the radiance from the completely cloud-covered portion. The radiance in any pixel is linearly proportional to the cloud-cover fraction of the pixel. The radiance for any pixel in the (250 km)^2 region is given by

$$I = (1 - A_c)I_s + A_c I_c \tag{1}$$

where A_c is the fractional cloud cover for the pixel, I_s the radiance associated with cloud-free portion, and I_c the radiance associated with the completely cloud-covered portion. By inverting (1), the fractional cloud cover is given by

$$A_c = \frac{I - I_s}{I_c - I_s} \tag{2}$$

The values of I_s and I_c are taken to be the mean radiances of the points that constitute the cloud-free and cloud-covered feet of the arch. These points can be identified automatically (Coakley and Bretherton, 1982).

Figure 3.1(b) shows the points that belong to the feet of the arch shown in Figure 3.1(a). The mean associated with a particular foot is given by

$$\bar{I} = \frac{1}{N}\sum_{n=1}^{N} I_n \tag{3}$$

and the standard deviation is given by

$$\sigma = \left\{ \frac{1}{N} \sum_{n=1}^{N} \left[\sigma_n^2 + (I_n - \bar{I})^2 \right] \right\}^{1/2} \tag{4}$$

where N is the number of 2×2 arrays associated with the foot, $4N$ the number of pixels, I_n the mean radiance for the n^{th} array and σ_n the standard deviation for the n^{th} array. For the data in Figure 3.1(b), the mean radiance for the points associated with the cloud-free foot is $I_s = 93.4$ mWm^{-2}sr^{-1}cm with a standard deviation of $\Delta I_s = 0.7$ mWm^{-2}sr^{-1}cm. The mean radiance for the cloud-covered foot is $I_c = 76.1$ mWm^{-2}sr^{-1}cm with a standard deviation of $\Delta I_c = 0.6$ mWm^{-2}sr^{-1}cm.

Since (1) is linear and since we assume that values of I_s and I_c remain unchanged for the entire (250 km)^2 region, it is not necessary to invert (1) to obtain the cloud-cover fraction for each pixel and then average these values to obtain the cloud-cover fraction for the (250 km)^2 region. Instead the mean radiance for the entire region can be used in (2) to obtain the cloud-cover fraction for the entire region. For the data in Figure 3.1(a), the mean (250km)^2 radiance is $I = 84.5$ mWm^{-2}sr^{-1}cm which combined with the associated values for $I_s = 93.4$ mWm^{-2}sr^{-1}cm and $I_c = 76.1$ mWm^{-2}sr^{-1}cm give the (250 km)^2 cloud-cover fraction, $A_c = 0.52$.

Coakley and Bretherton also illustrated that the uncertainty in A_c can be estimated from the uncertainty associated with I_s and I_c, that is, ΔI_s, the standard deviation associated with the cloud-free foot, and ΔI_c, the standard deviation associated with the cloud-covered foot. The uncertainty in cloud cover can be derived from (2) and is given by

$$\Delta A_c = \pm \left\{ \left(\frac{A_c \Delta I_c}{I_c - I_s} \right)^2 + \left[\frac{(1 - A_c)\Delta I_s}{I_c - I_s} \right]^2 \right\}^{1/2} \tag{5}$$

For the case in Figure 3.1(a), the uncertainty in cloud cover, ΔA_c, is ~0.03.

As is the case with many of the other techniques developed for deducing cloud cover, the spatial coherence method has some obvious limitations. The spatial coherence method detects a cloud layer only when the cloud layer emits locally uniform radiances. Hence, to detect the cloud layer, several adjacent pixels within

a localized region must be completely filled by a uniform layered cloud. Thus, the method fails when the clouds are everywhere smaller than the instrument's field of view, and when the clouds have variable emissivities, as do cirrus clouds. But the spatial coherence method also identifies systems for which failure is imminent, i.e., no cloud-covered foot. Also, because multilayered systems require the determination of fractional coverage in each of the layers, they are more complicated than single-layered systems in determining cloud cover. In order to use the spatial coherence method retrieved cloud cover as a "truth" set, it is necessary to use only cases for which the clouds form single-layered systems.

Figures 3.2–3.5 are all for nighttime passes over the southern Pacific ocean in April 1985. Each figure represents a (250 km)^2 area. These figures illustrate inappropriate cases identified so by the spatial coherence method. Figure 3.2a shows an arch for a two-layered system while Figure 3.2b shows an arch for a three-layered system. Although an extension of the spatial coherence method that allows for the treatment of multilayered cloud systems by using simultaneous observations at 3.7 μm and 11 μm infrared channels has also been developed (Coakley, 1983), the large uncertainties intrinsic to complex multilayered systems forces their exclusion in this study. Figure 3.3 also shows an arch for a single-layered system, but in 3.3a the standard deviation associated with the cloud-free foot is quite large and similarly in 3.3b the standard deviation associated with the cloud-covered foot is large. As mentioned previously, these large standard deviations will produce large uncertainties ($> \pm 10\%$) in the derived cloud cover. In Figure 3.4 the number of 2×2 pixel arrays in either the cloud-free foot or cloud-covered foot are insufficient to construct a specific foot of the arch, whereas Figure 3.5 shows that a low-level cloud deck and a high-level layer, probably cirrus, are present simultaneously. Cirrus clouds are rarely detected as a layer due to their variable emissivities. These cases do not belong to the set of single-layered systems. The spatial coherence method, as do all current methods, fails to obtain accurate cloud cover for such complex systems.

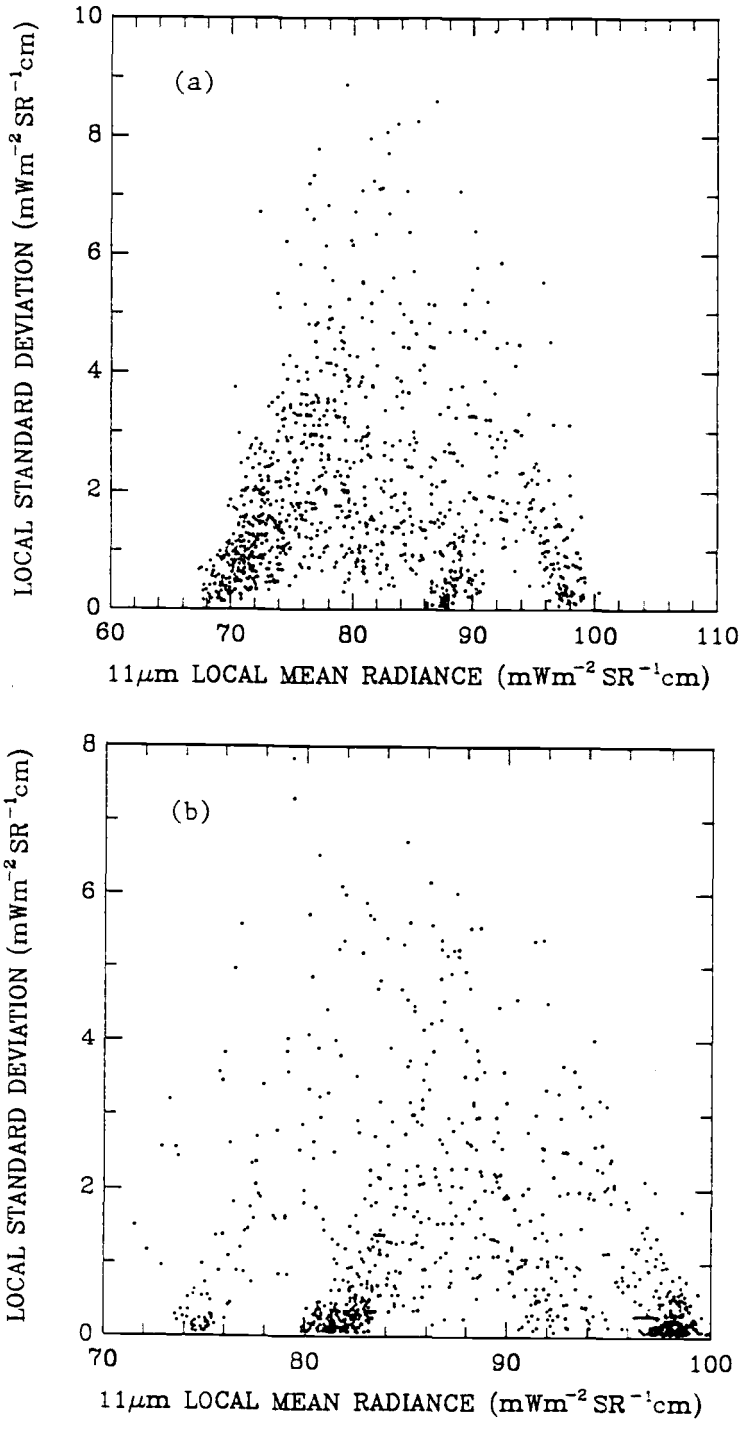

Figure 3.2 (a) Local means and local standard deviations of 11μm radiances for 2×2 (scan spot × scan line) arrays of GAC (4 km)^2 NOAA-9 AVHRR pixels. The data are for the nighttime pass over a (250 km)^2 region of the Pacific Ocean centered at 7.4°S, 93.0°W, on April 9, 1985. (b) Same as (a) except for the region centered at 9.4°S, 83.9°W on April 19, 1985.

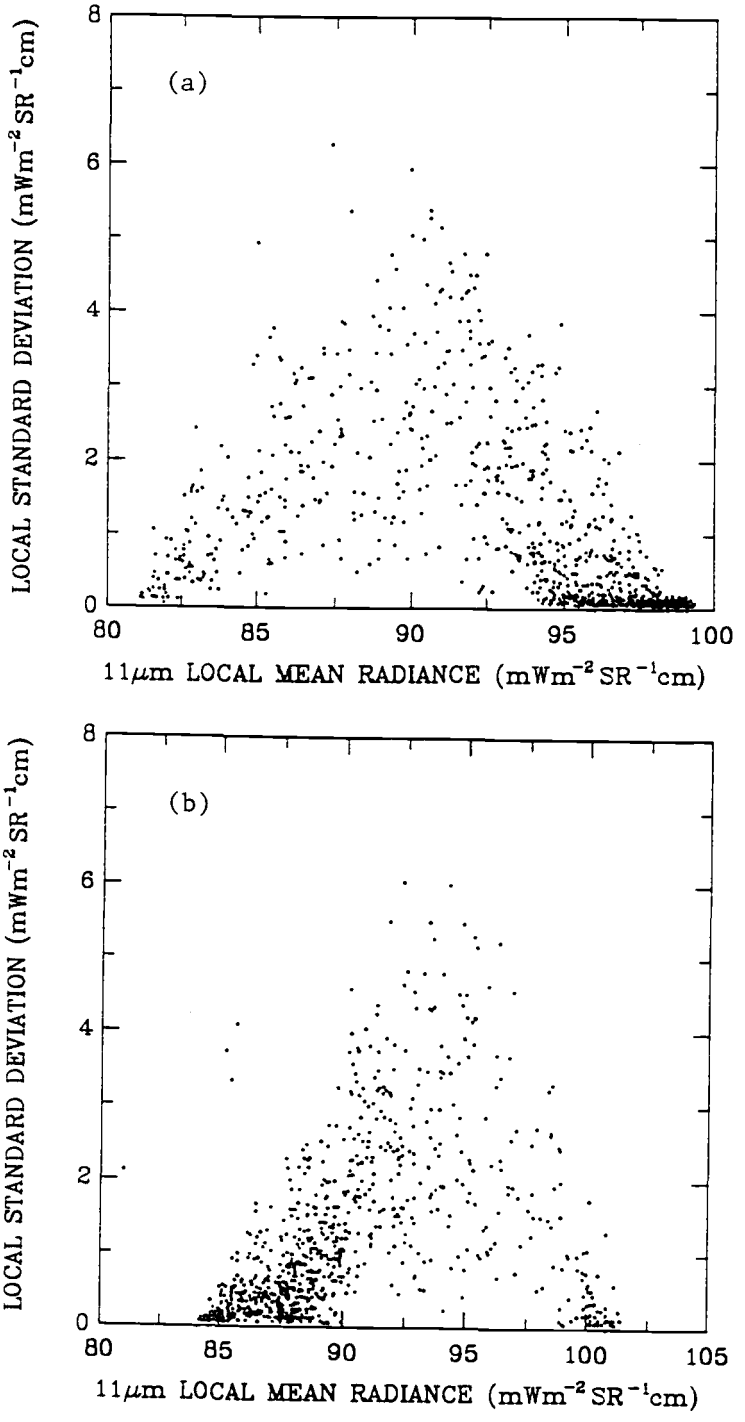

Figure 3.3 (a) Local means and local standard deviations of 11μm radiances for 2×2 (scan spot × scan line) arrays of GAC (4 km)^2 NOAA-9 AVHRR pixels. The data are for the nighttime pass over a (250 km)^2 region of the Pacific Ocean centered at 22.1°S, 88.9°W, on April 9, 1985. (b) Same as (a) except for the region centered at 20.5°S, 86.2°W on April 19, 1985.

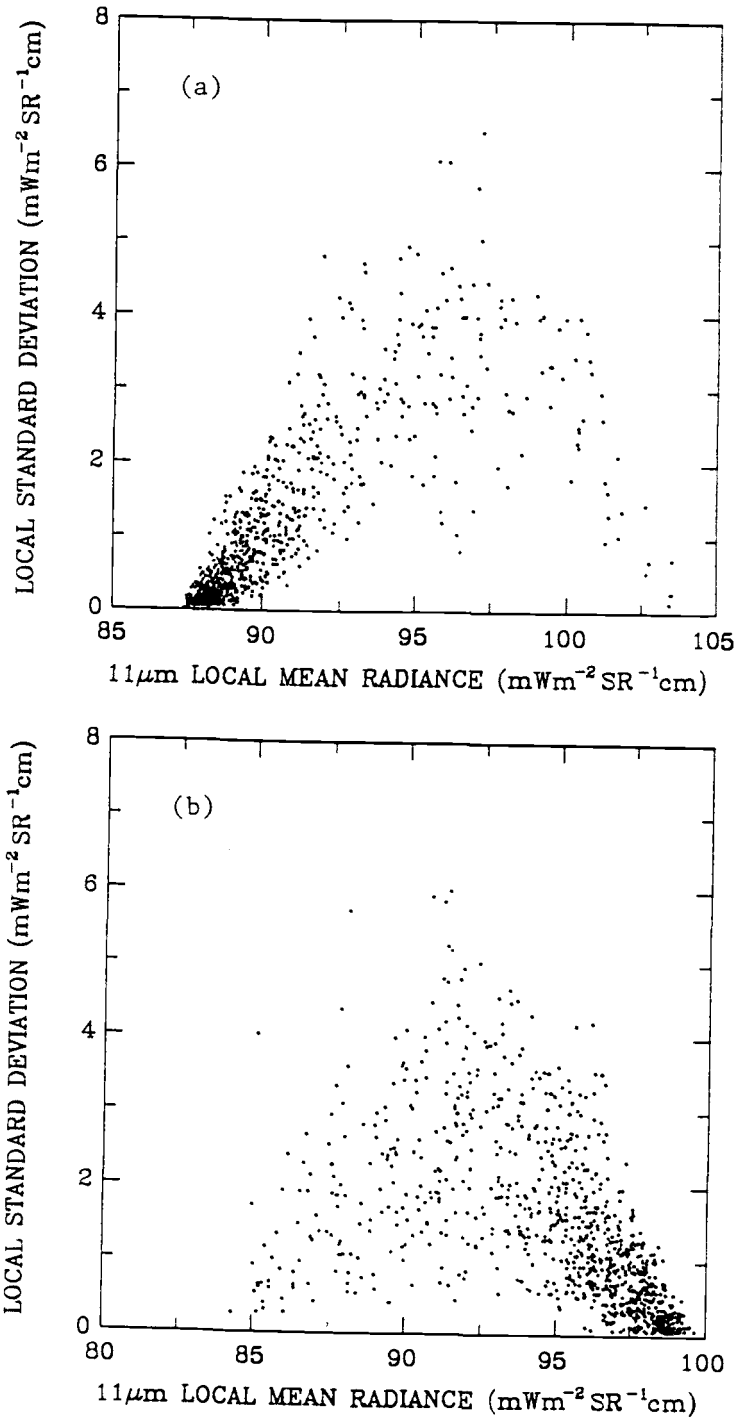

Figure 3.4 (a) Local means and local standard deviations of 11μm radiances for 2×2 (scan spot × scan line) arrays of GAC (4 km)^2 NOAA-9 AVHRR pixels. The data are for the nighttime pass over a (250 km)^2 region of the Pacific Ocean centered at 17.4°S, 94.9°W, on April 19, 1985. (b) Same as (a) except for the region centered at 22.4°S, 104.4°W on April 19, 1985.

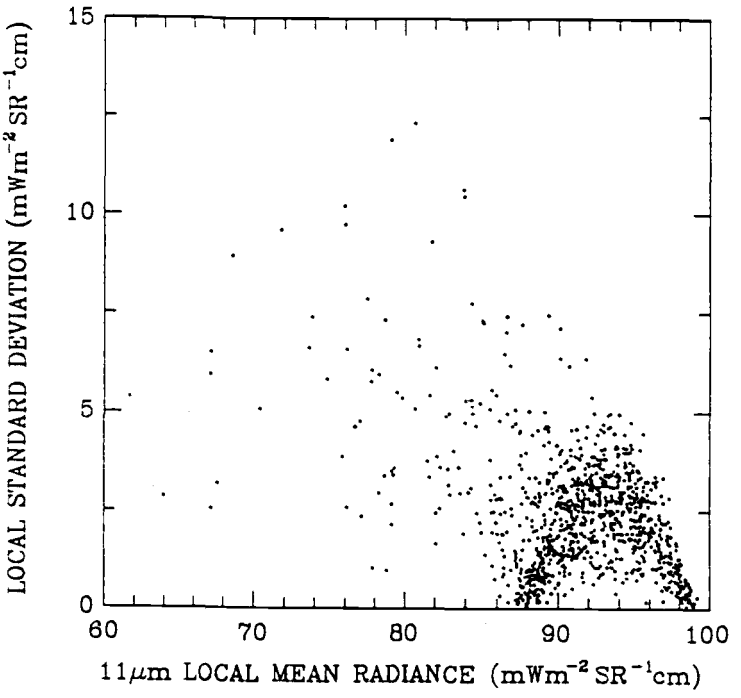

Figure 3.5 Local means and local standard deviations of 11μm radiances for 2×2 (scan spot × scan line) arrays of GAC (4 km)^2 NOAA-9 AVHRR pixels. The data are for the nighttime pass over a (250 km)^2 region of the Pacific Ocean centered at 25.7°S, 94.4°W, on April 19, 1985.

4. Data Analysis

Both threshold and spatial coherence methods were applied to NOAA-9 AVHRR global area coverage satellite imagery data. The data was obtained from the ERBE V-5 Scene Identification Validation Data Set. The V-5 data contain observations from ten-minute orbital segments taken from selected geographical locations. The AVHRR scans perpendicularly to the direction of the orbit and its resolution is approximately $(4\ \text{km})^2$ at nadir. The AVHRR carries five channels, a visible channel, 0.63μm, a near infrared channel, 0.89μm, and three infrared channels, 3.7μm, 11μm, 12μm. In this study, only the 11μm infrared channel radiances are analyzed. The 11μm channel was selected for the spatial coherence analyses because clouds are often opaque at 8–12μm; and therefore the infrared emission from overcast layered clouds is spatially uniform. By comparison, at visible wavelengths clouds are not opaque and consequently the reflection of sunlight rarely achieves spatial uniformity even for extensive layered cloud systems.

Several V-5 regions were collected by ERBE. Each V-5 region covers a geographic area of approximately (2900 km $\times$ 4800 km). Four V-5 regions, 0644, 0837, 1197, and 1566, are selected for study. As shown in Figure 4.1, region 0644 covers the northern Atlantic Ocean; region 0837 covers the northeastern Pacific Ocean; region 1197 covers the middle Pacific Ocean; and region 1566 covers the southeastern Pacific Ocean. There are three reasons for selecting oceanic regions. First, oceans provide a nearly homogeneous surface on a spatial scale of approximately $(100\ \text{km})^2$ which does not change rapidly in time. Consequently, the clear sky radiances over the ocean are nearly constant over a $\sim(250\ \text{km})^2$ area. By comparison, complex terrain and the variety of surface types cause land to be a spatially inhomogeneous emitter. Second, the weather conditions over oceans do not produce as many complicated cloud types as do those over land. This study is limited to single-layered cloud systems for which the spatial coherence method is expected to produce accurate cloud cover. Such single-

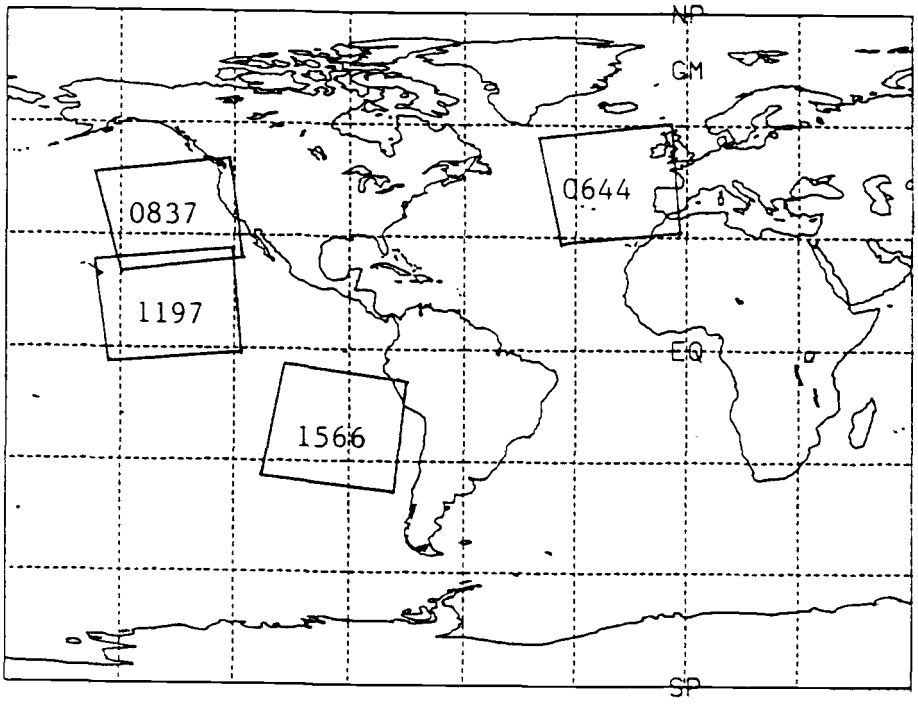

Figure 4.1 V-5 regions used in this study.

layered systems are common and they often extend over several hundred to even a thousand kilometers. Third, the regions selected for study represent tropics, subtropics, and mid-latitudes and thus provide a variety of climatological conditions.

The data used in this study were taken from nighttime passes on 18 different days in April, July, and October, 1985 over the four regions. The 18 different days are shown in Table 1. There are six days in each month. In the data analysis a V-5 region

Table 1. Dates selected in this study

	1985
April	4, 9, 14, 19, 24, 29
July	3, 8, 13, 18, 23, 28
October	1, 6, 11, 16, 21, 26

is divided into four subregions with the geographic area of each subregion being approximately (2450 km × 1000 km). We call the subregion a scene.

Figure 4.2 illustrates the satellite geometry. The figure shows the orientation of the AVHRR scan lines and scan spots with respect to the subsatellite orbital track. The array is 384 scan spots wide and 256 scan lines long. The scene is subdivided into 6×4 frames, 64 scan spots by 64 scan lines each. Each frame is approximately $(250 \text{ km})^2$ at nadir. Also, each frame is divided into 4×4 sub-frames, 16 scan spots by 16 scan lines. Each sub-frame is approximately $(60 \text{ km})^2$ at nadir. The spatial coherence method uses the local means and standard deviations of the radiances for each 2×2 pixel array. There are 32×32 arrays in a frame and 8×8 in a sub-frame.

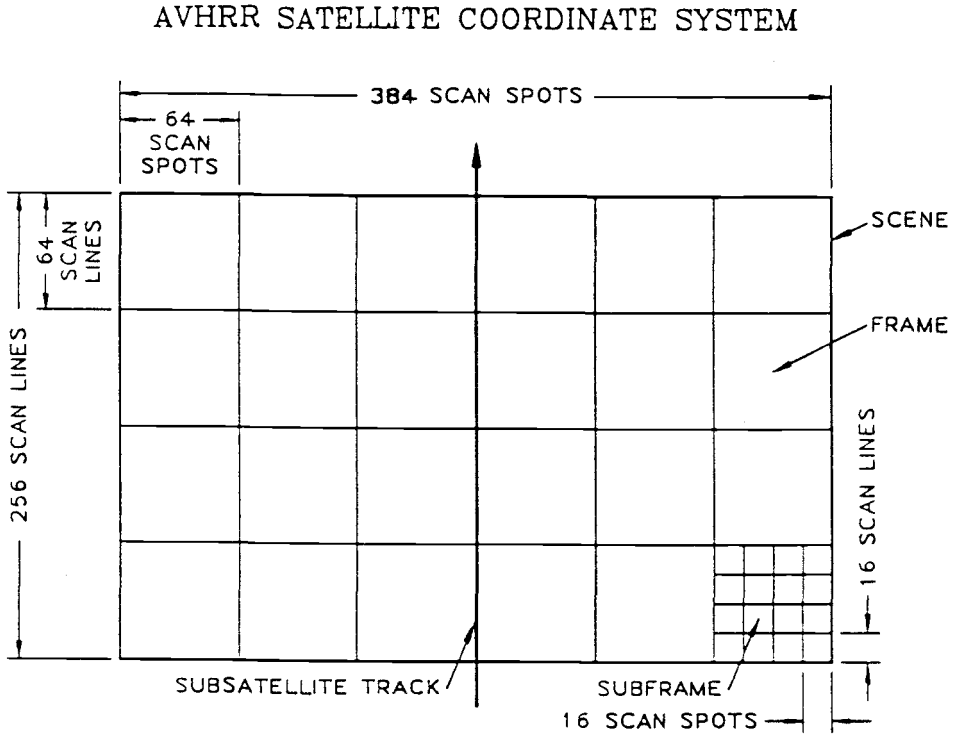

Figure 4.2 Satellite scene, frame, and sub-frame. There are four such scenes in each pass over a V-5 region. The scene covers a geographical area of approximately (2450 km × 1000 km), a frame $(250 \text{ km})^2$ at nadir, and a subframe $(60 \text{ km})^2$ at nadir.

As the cloud cover derived by the ISCCP is for each $\sim(250\ \text{km})^2$ area, the threshold and spatial coherence analyses are processed on the frame scale. For comparison, they are also processed on the sub-frame scale in this study. Because accurate retrievals using the spatial coherence method are expected only for single-layered cloud systems, only those frames and sub-frames which have been identified as having single-layered systems are selected for study. The results of the spatial coherence analysis identifies the appropriate single-layered system.

An appropriate single-layered system is defined by 1) only one cloud-covered foot is present in a typical spatial coherence analyzed arch (as shown in Figure 3.1); 2) the number of 2×2 pixel arrays is enough to constitute a significant cloud-covered foot; 3) the standard deviations associated with the cloud-free foot and cloud-covered foot are less than 2.5 $\text{mWm}^{-2}\text{sr}^{-1}\text{cm}$. This number gives an uncertainty of $\Delta A_c \sim 0.09$ for the spatial coherence retrieved $A_c = 0.5$ and $I_s - I_c = 20\ \text{mWm}^{-2}\text{sr}^{-1}\text{cm}$; and 4) no high-level cirrus cloud is present, that is, none of the local mean 11μm radiance of 2×2 array pixels is lower than the radiance range associated with the cloud-covered foot. With these restrictions, the spatial coherence method retrieved cloud-cover fraction should represent a realistic "cloud truth" data set.

5. Comparison of Cloud Cover Obtained by the Spatial Coherence and Threshold Methods

In order to obtain threshold derived cloud cover, three different values of the threshold for the 11μm infrared radiances are selected. The three different thresholds are set to be: 1) the cloud-free threshold - which is at a radiance near the cloud-free radiance and is given by the cloud-free radiance (I_s) minus three times the standard deviation of the cloud-free radiance (ΔI_s), i.e., $I_s - 3\Delta I_s$; 2) the midpoint threshold - which is at the arithmetic mean of the cloud-free radiance and the cloud-covered radiance (I_c), i.e., $(I_s + I_c)/2$; 3) the overcast threshold - which is at a radiance near the cloud-covered radiance and is given by the cloud-covered radiance plus three times the standard deviation of the cloud-covered radiance (ΔI_c), i.e., $I_c + 3\Delta I_c$. Here the cloud-free threshold is the conventional threshold that is currently used by most of the cloud-retrieval programs. The midpoint and overcast thresholds are selected for test and comparison.

Figure 5.1 illustrates the setting of these thresholds. The data in Figure 5.1 are the same as those shown in Figure 3.1. The derived mean cloud-free radiance in the figure is $I_s = 93.4$ mWm^{-2}sr^{-1}cm with the standard deviation $\Delta I_s = 0.7$ mWm^{-2}sr^{-1}cm and the mean cloud-covered radiance is $I_c = 76.1$ mWm^{-2}sr^{-1}cm with the standard deviation $\Delta I_c = 0.6$ mWm^{-2}sr^{-1}cm. So, the three thresholds are calculated to be 1) $I_s - 3\Delta I_s = 91.5$ mWm^{-2}sr^{-1}cm; 2) $(I_s + I_c)/2 = 84.8$ mWm^{-2}sr^{-1}cm; 3) $I_c + 3\Delta I_c = 77.9$ mWm^{-2}sr^{-1}cm.

These three thresholds are applied to each field of view and all image pixels are classified as clear or cloudy according to whether the measured radiance I of a pixel is greater than the predetermined threshold, e.g., $I_s - 3\Delta I_s$, $(I_s + I_c)/2$, or $I_c + 3\Delta I_c$. The cloud-cover fraction is then given by the ratio of the number of cloudy pixels to the number of total pixels in each frame or sub-frame.

Figure 5.2(a), (b), (c) respectively show cloud-cover fractions obtained with

three different thresholds, as described above, compared with those derived by the spatial coherence method over four regions. Each point gives both the spatial coherence and threshold method analyzed cloud-cover fractions for the selected (60 km)^2 sub-frames extracted from a V–5 region. The area extracted is approximately (2450 km $\times$ 4000 km). The cloud-free radiance, I_s, and cloud-covered radiance, I_c, are determined for each (250 km)^2 frame. The cloud-cover fraction for each (60 km)^2 sub-frame is determined by the I_s and I_c of a (250 km)^2 frame that contains the sub-frame.

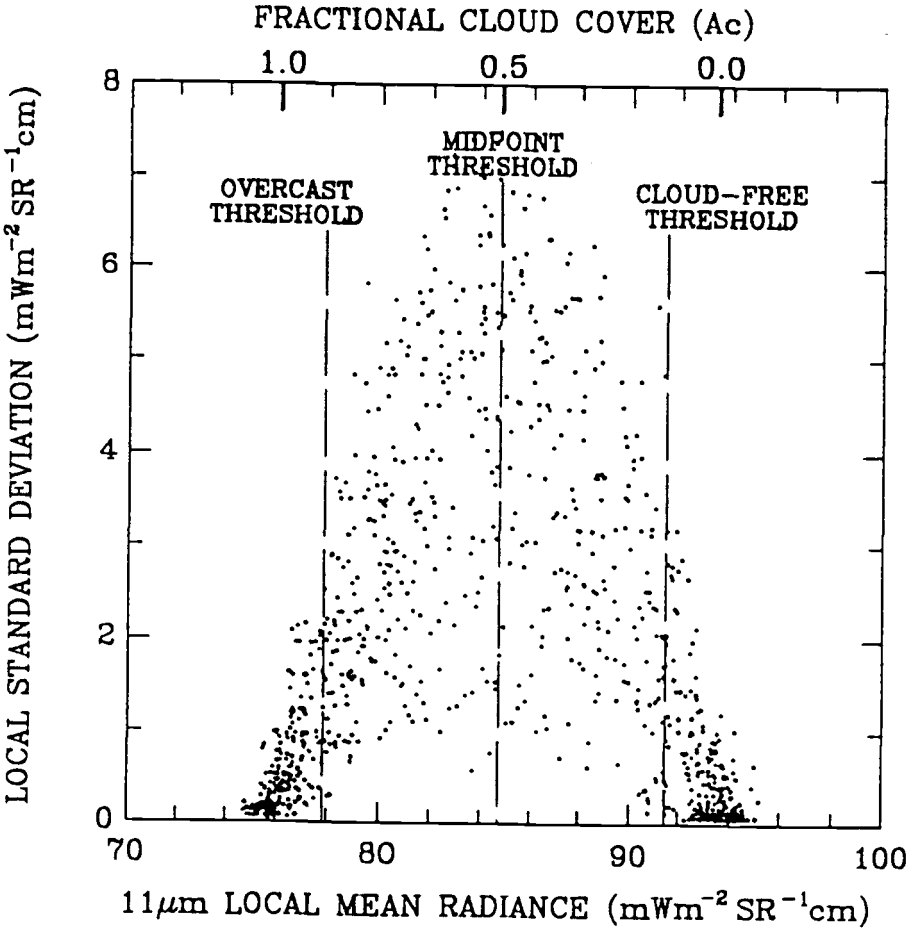

Figure 5.1 The data is the same as in Figure 3.1. The axis at the top of the figure indicates the fractional cloud cover. The dash lines indicate the placement of the cloud-free, midpoint, and overcast thresholds, as described in the text.

Likewise, Figure 5.3(a), (b), (c) are all plotted in the same manner as Figure 5.2 except that each point gives the cloud-cover fraction for a (250 km)^2 frame. The number of points in Figure 5.3(a), (b), (c) representing the (250 km)^2 scale are fewer than those in Figure 5.2(a), (b), (c) representing the (60 km)^2 scale. The points in these figures with cloud-cover fractions near 1.0 (scattered near the upper right corner of each diagram) represent the extensively overcast sub-frames or frames and those with cloud-cover fractions near 0.0 (scattered near the lower left corner of each diagram) represent the extensively cloud-free frames or sub-frames.

In comparison with the spatial coherence results in frame and sub-frame scales, setting the threshold at $I_s - 3\Delta I_s$ tends to produce higher estimates of cloud-cover fraction, as shown in Figure 5.2(a) and 5.3(a), and setting the threshold at $I_c + 3\Delta I_c$ tends to produce lower estimates of cloud-cover fraction, as shown in Figure 5.2(c) and 5.3(c). Setting the threshold at $(I_s + I_c)/2$ appears to give small differences, as shown in Figure 5.2(b) and 5.3(b). Also the results associated with the overcast threshold appears to be the mirror image of those associated with the cloud-free threshold. The differences are shown in Figure 5.4(a), (b), (c) and 5.5(a), (b), (c) as the threshold estimates of cloud-cover fraction minus the spatial coherence estimates of cloud-cover fraction and are plotted as a function of the spatial coherence derived fractional cloud cover.

The figures associated with the cloud-free and overcast thresholds show that the differences increase to maximum values ($\sim$0.18 for frame and $\sim$0.24 for subframe) when the cloud-cover fraction approaches 0.5. However, for those figures associated with the midpoint threshold the differences are found to be comparatively small, with the threshold method giving smaller estimates of cloud-cover fraction than the spatial coherence method when the cloud-cover fractions are less than $\sim$0.5 and larger estimates when the cloud-cover fractions are greater than $\sim$0.5. These small differences can be explained as follows: for a frame or sub-frame with a cloud-cover fraction of less than 0.5, most of the partially covered pixels have a fractional cloud

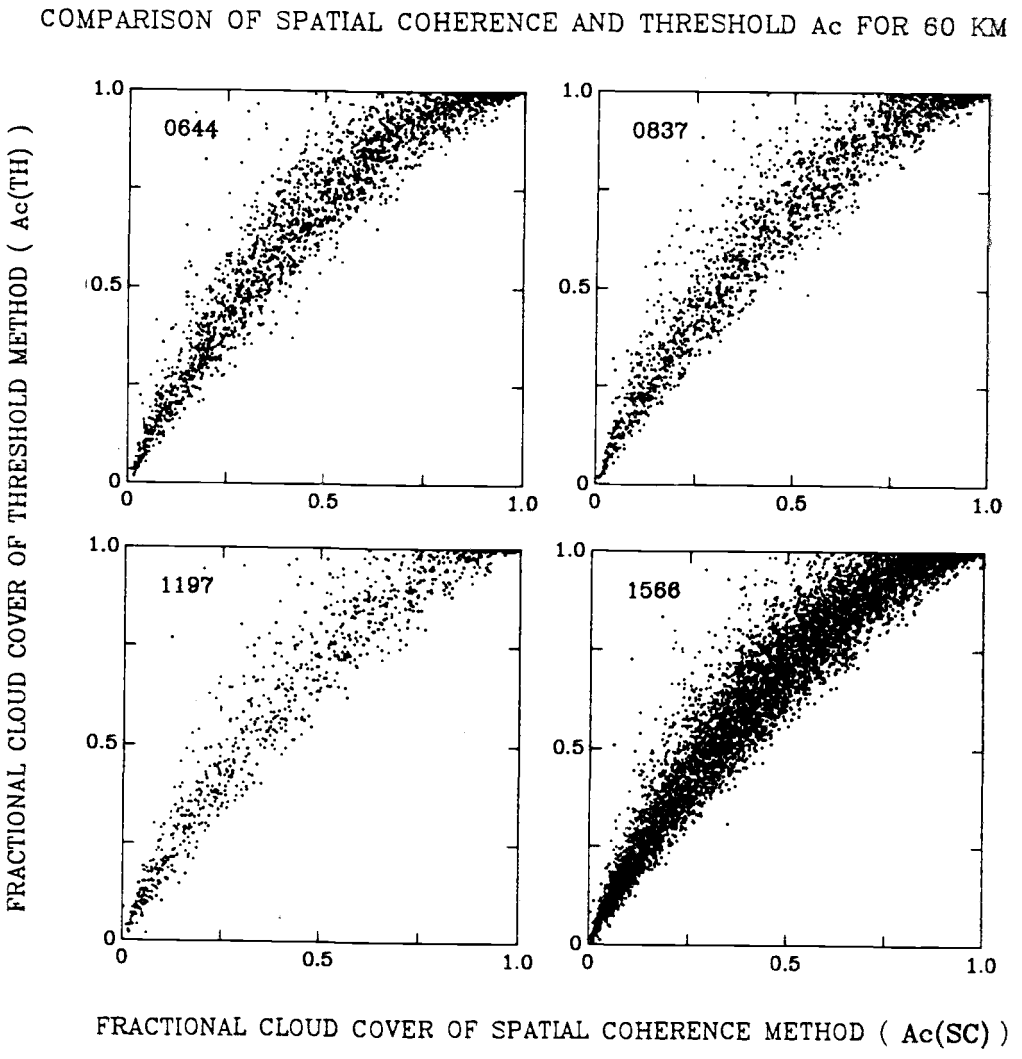

Figure 5.2(a) Comparison of cloud cover obtained by the spatial coherence and the cloud-free threshold method. Each point is for a subframe which at nadir has an area of approximately (60 km)^2.

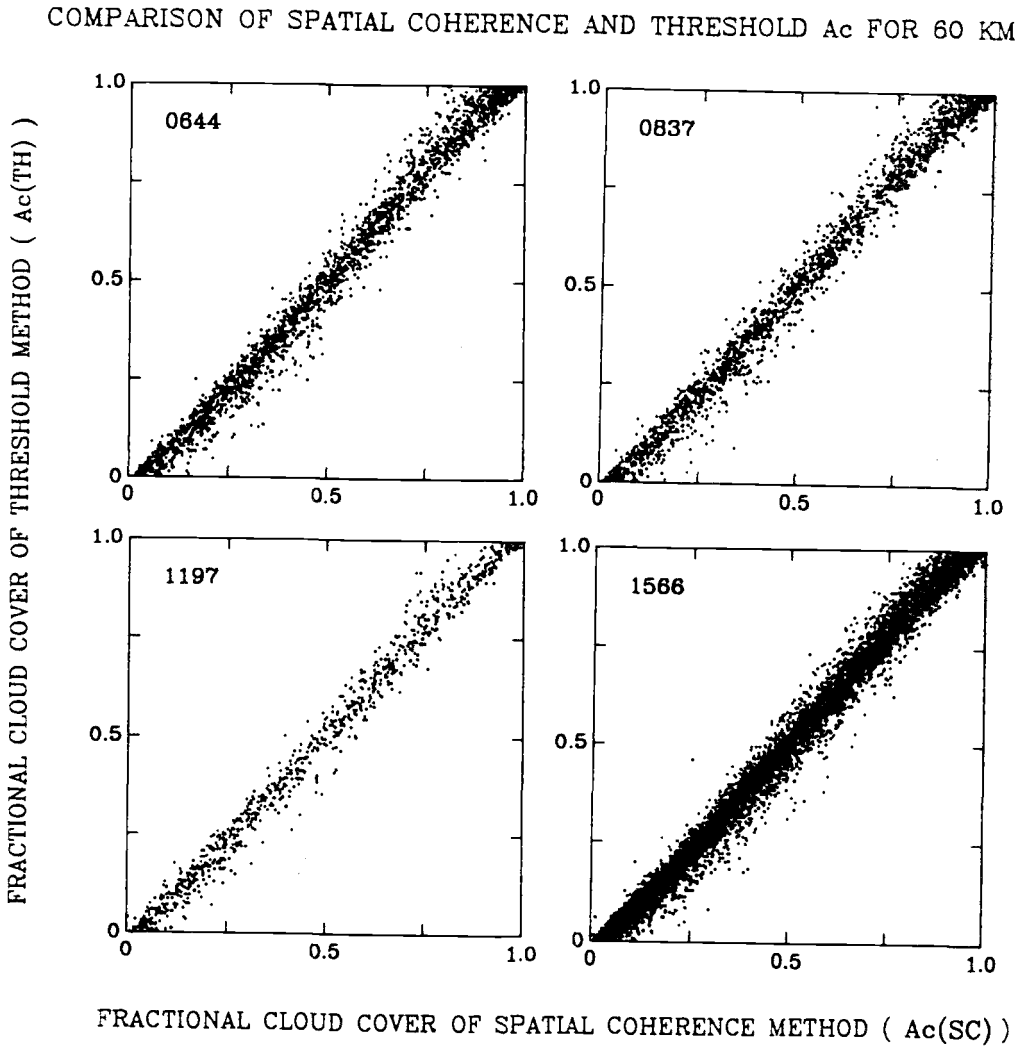

Figure 5.2(b) Comparison of cloud cover obtained by the spatial coherence and the midpoint threshold method. Each point is for a subframe which at nadir has an area of approximately $(60\ km)^2$.

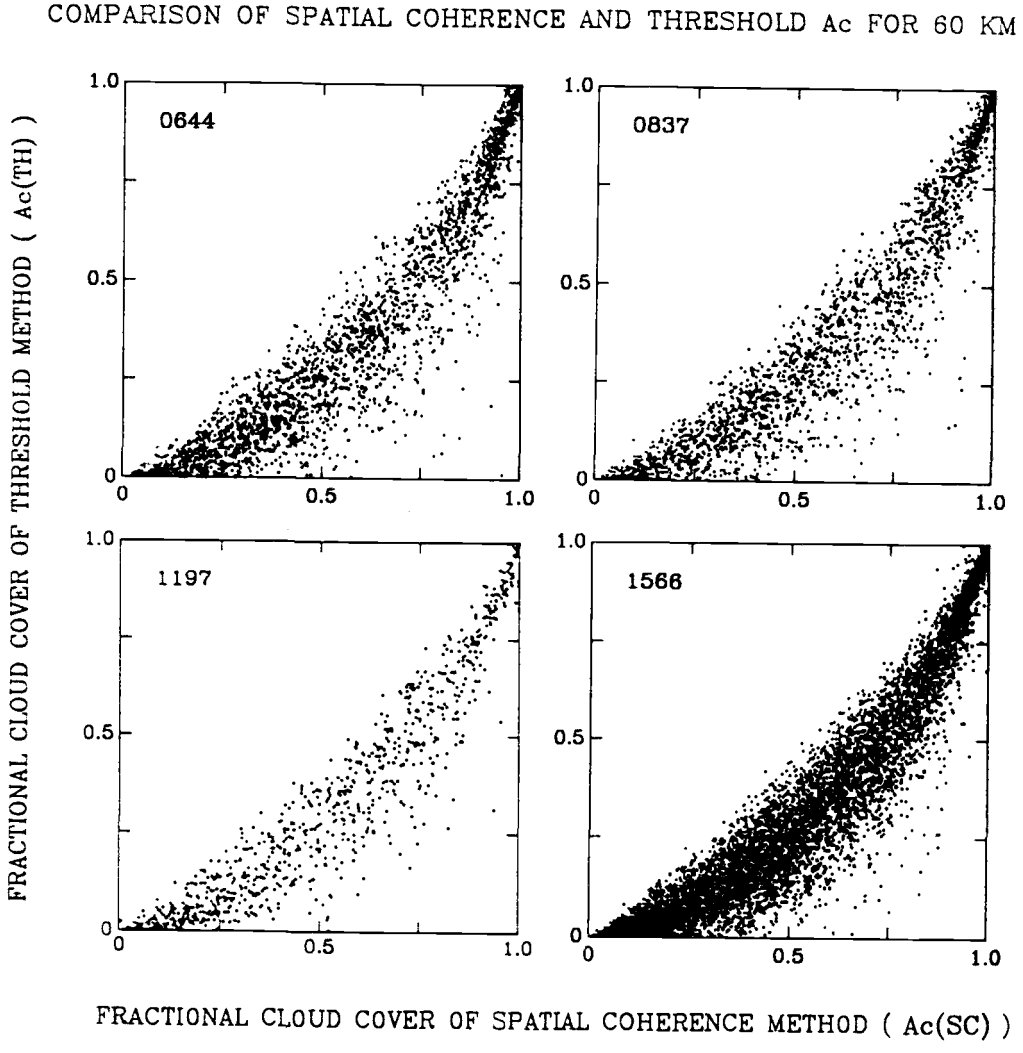

Figure 5.2(c) Comparison of cloud cover obtained by the spatial coherence and the overcast threshold method. Each point is for a subframe which at nadir has an area of approximately (60 km)^2.

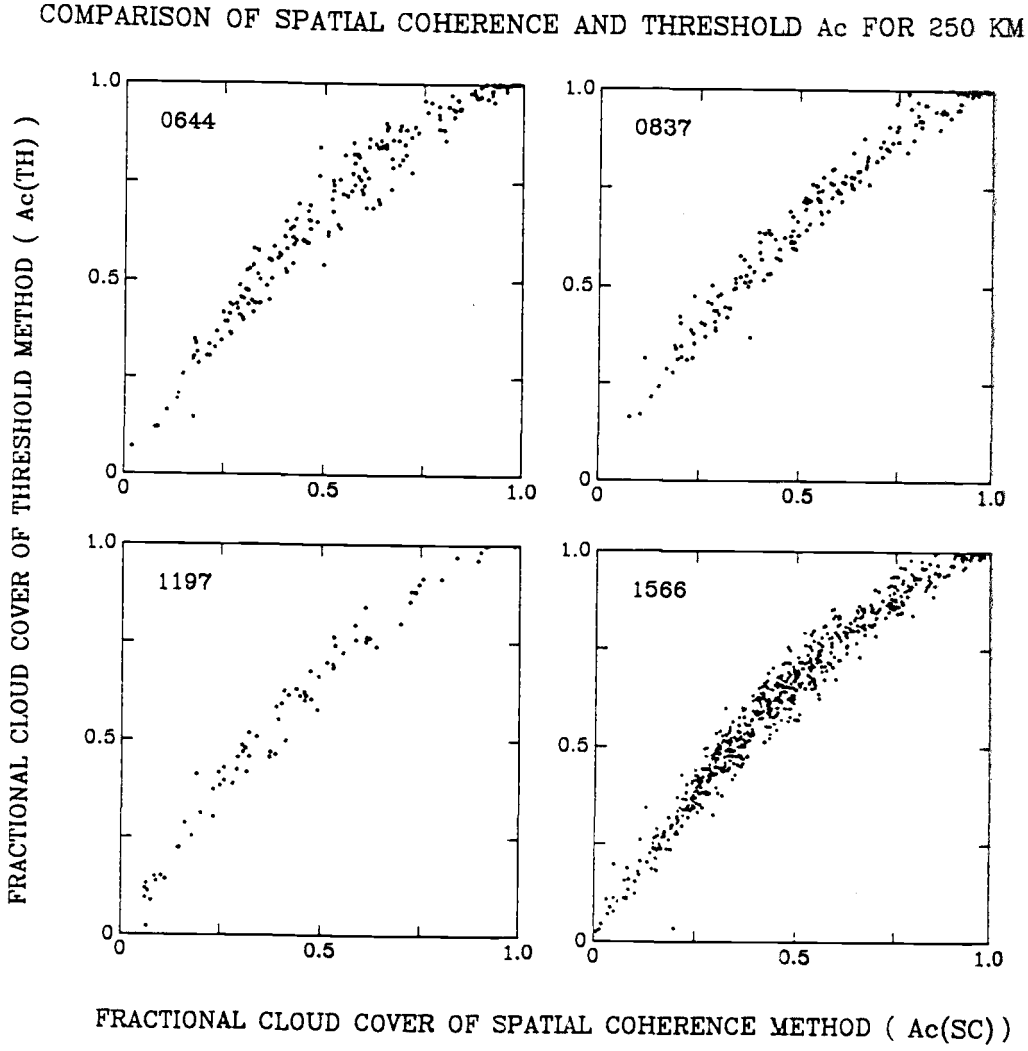

Figure 5.3(a) Comparison of cloud cover obtained by the spatial coherence and the cloud-free threshold method. Each point is for a frame which at nadir has an area of approximately (250 km)^2.

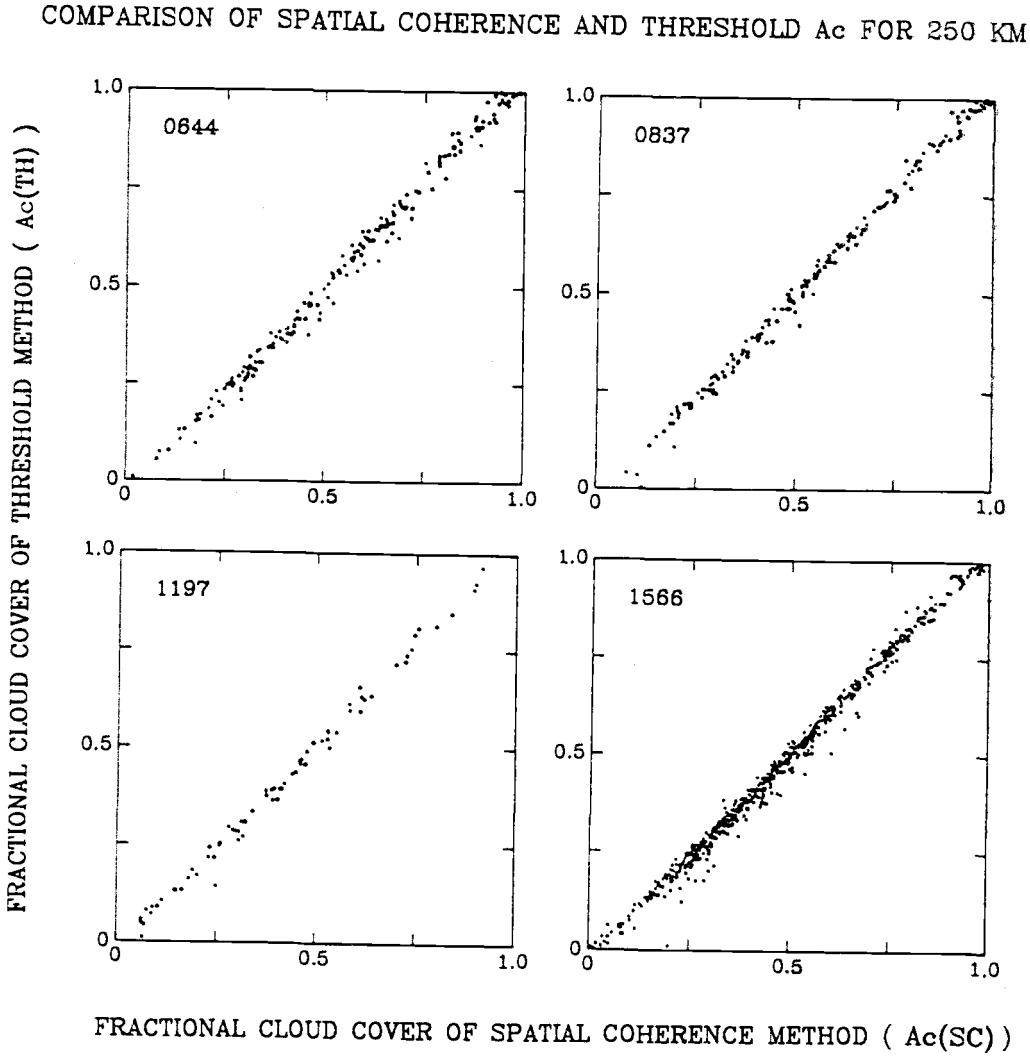

Figure 5.3(b) Comparison of cloud cover obtained by the spatial coherence and the midpoint threshold method. Each point is for a frame which at nadir has an area of approximately (250 km)^2.

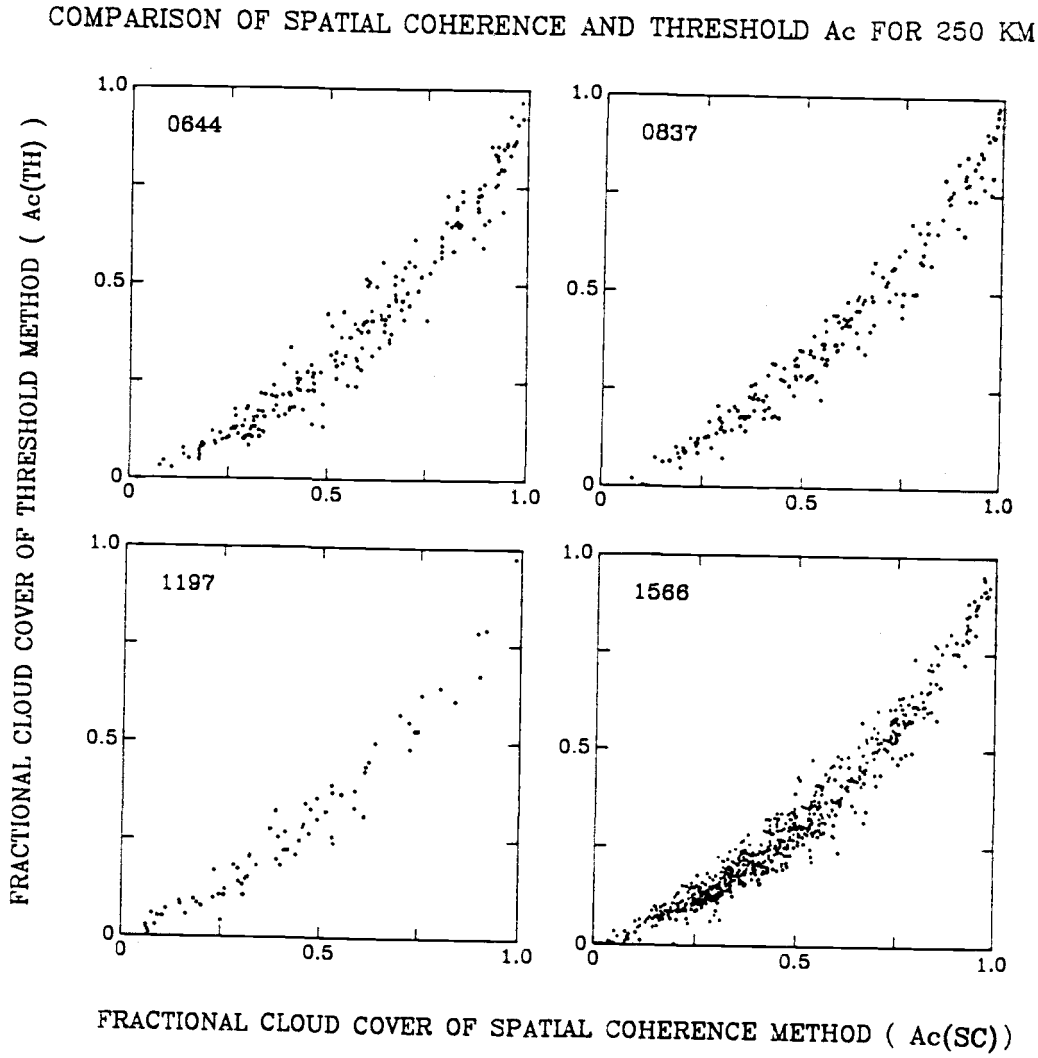

Figure 5.3(c) Comparison of cloud cover obtained by the spatial coherence and the overcast threshold method. Each point is for a frame which at nadir has an area of approximately (250 km)^2.

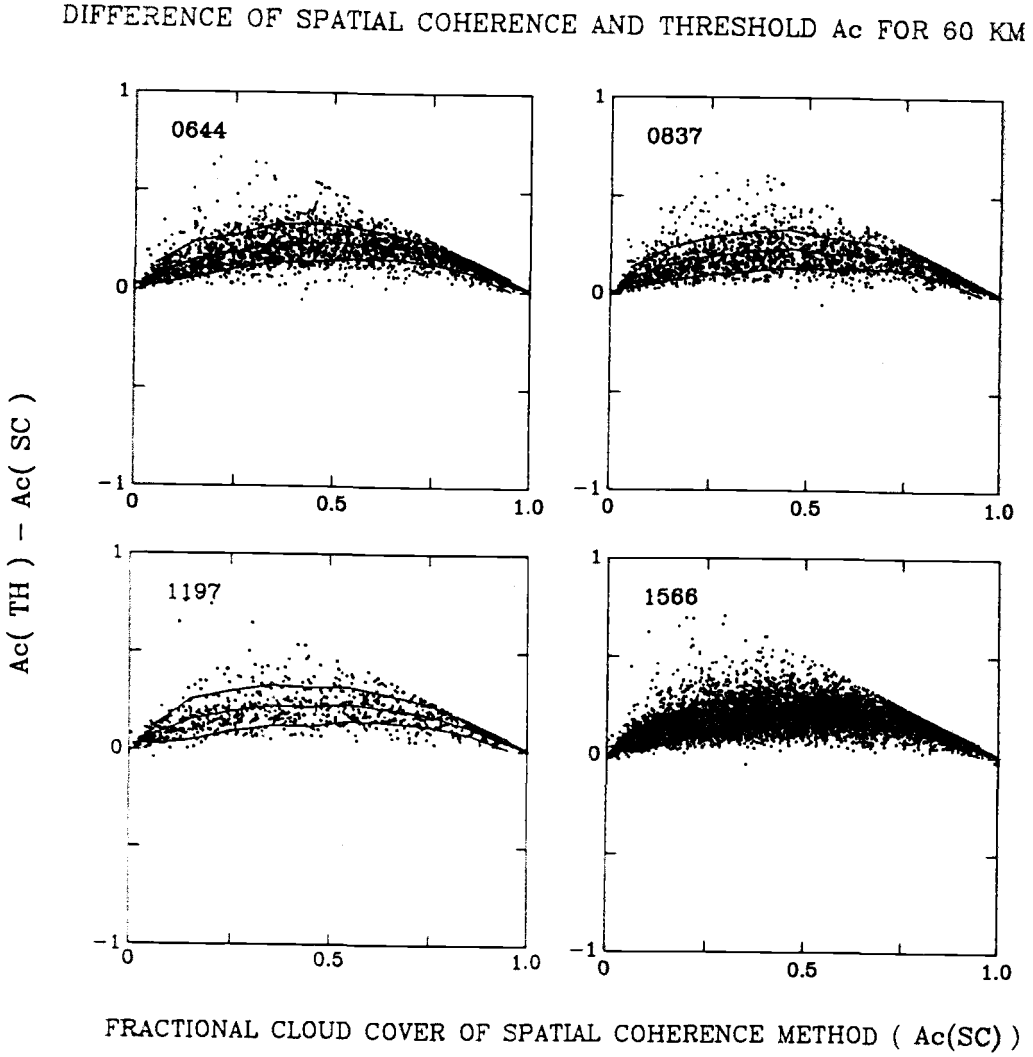

Figure 5.4(a) Differences in cloud cover obtained with the spatial coherence and the cloud-free threshold method. Each point is for a subframe which at nadir has an area of approximately (60 km)^2.

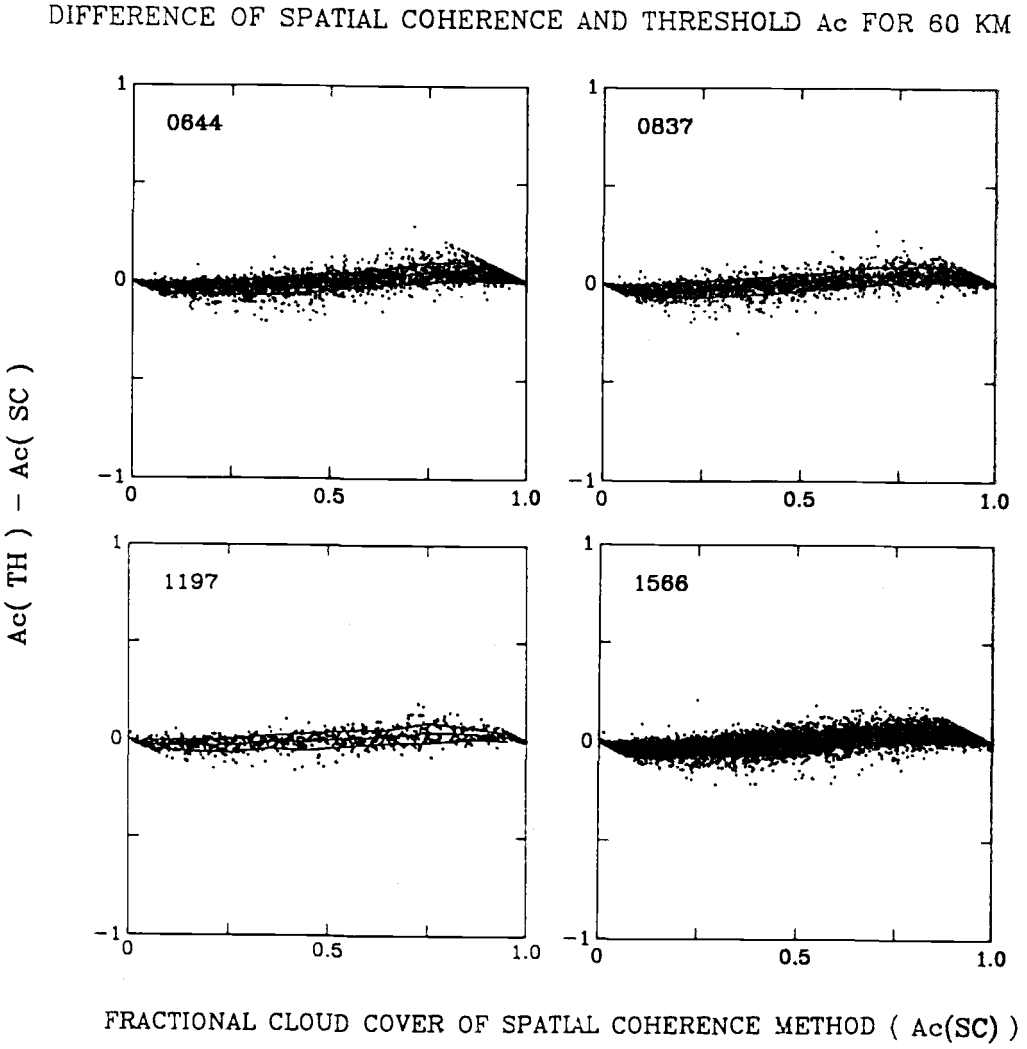

Figure 5.4(b) Differences in cloud cover obtained with the spatial coherence and the midpoint threshold method. Each point is for a subframe which at nadir has an area of approximately (60 km)^2.

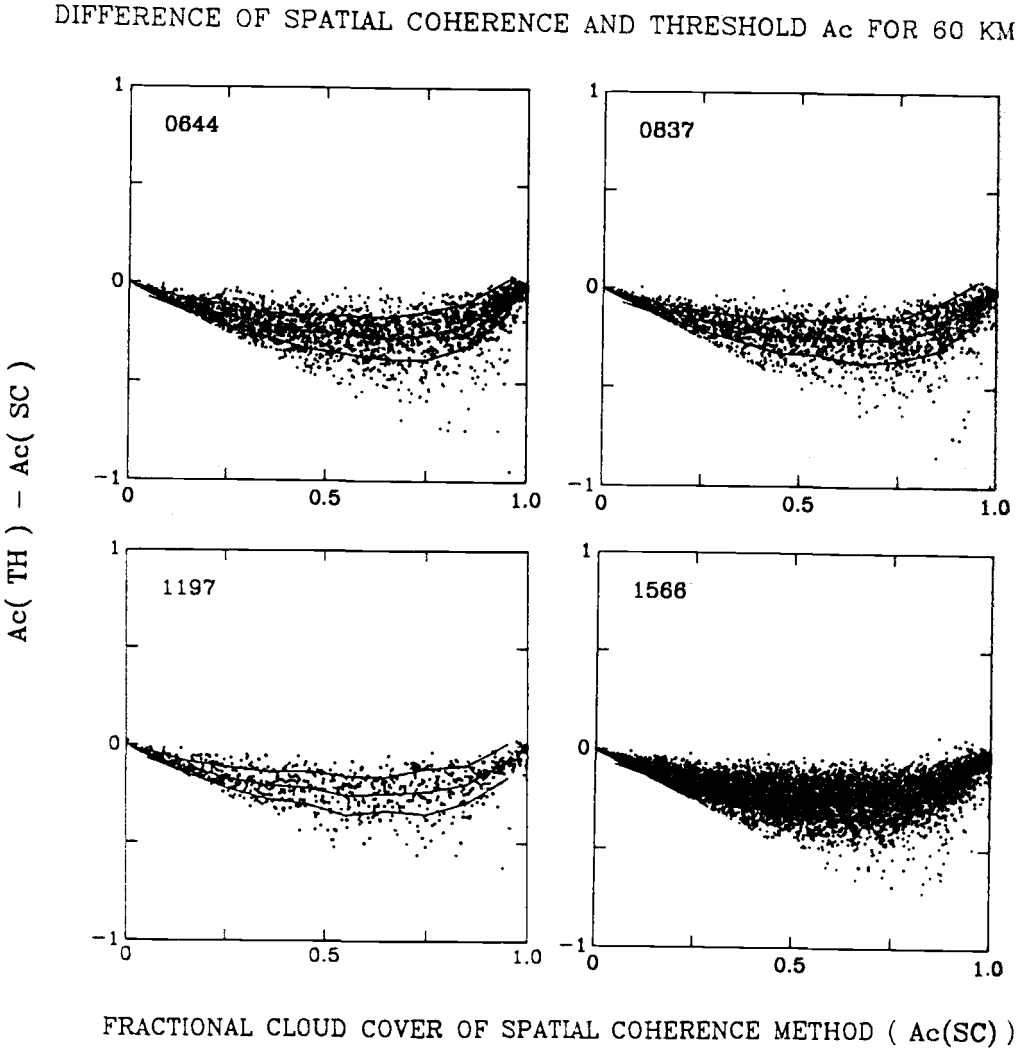

Figure 5.4(c) Differences in cloud cover obtained with the spatial coherence and the overcast threshold method. Each point is for a subframe which at nadir has an area of approximately (60 km)^2.

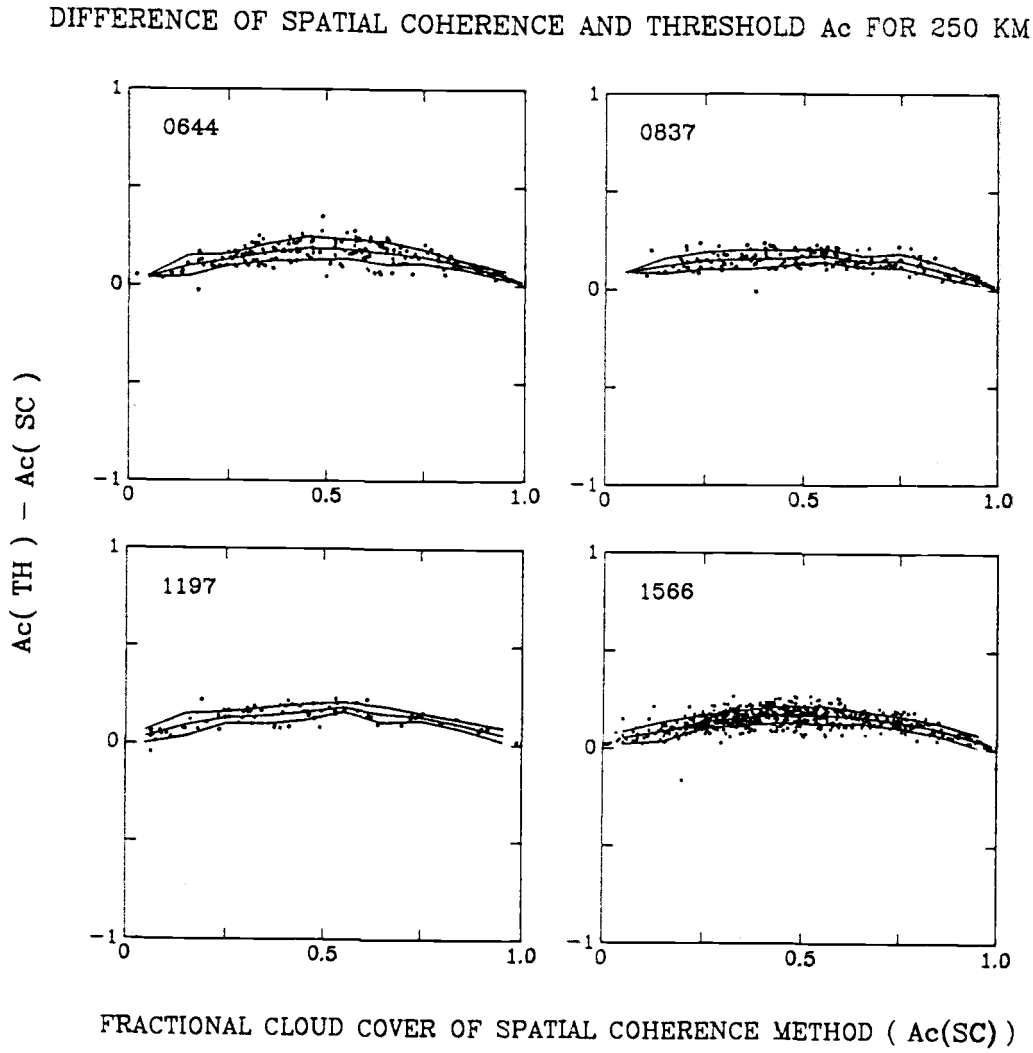

Figure 5.5(a) Differences in cloud cover obtained with the spatial coherence and the cloud-free threshold method. Each point is for a frame which at nadir has an area of approximately $(250\ km)^2$.

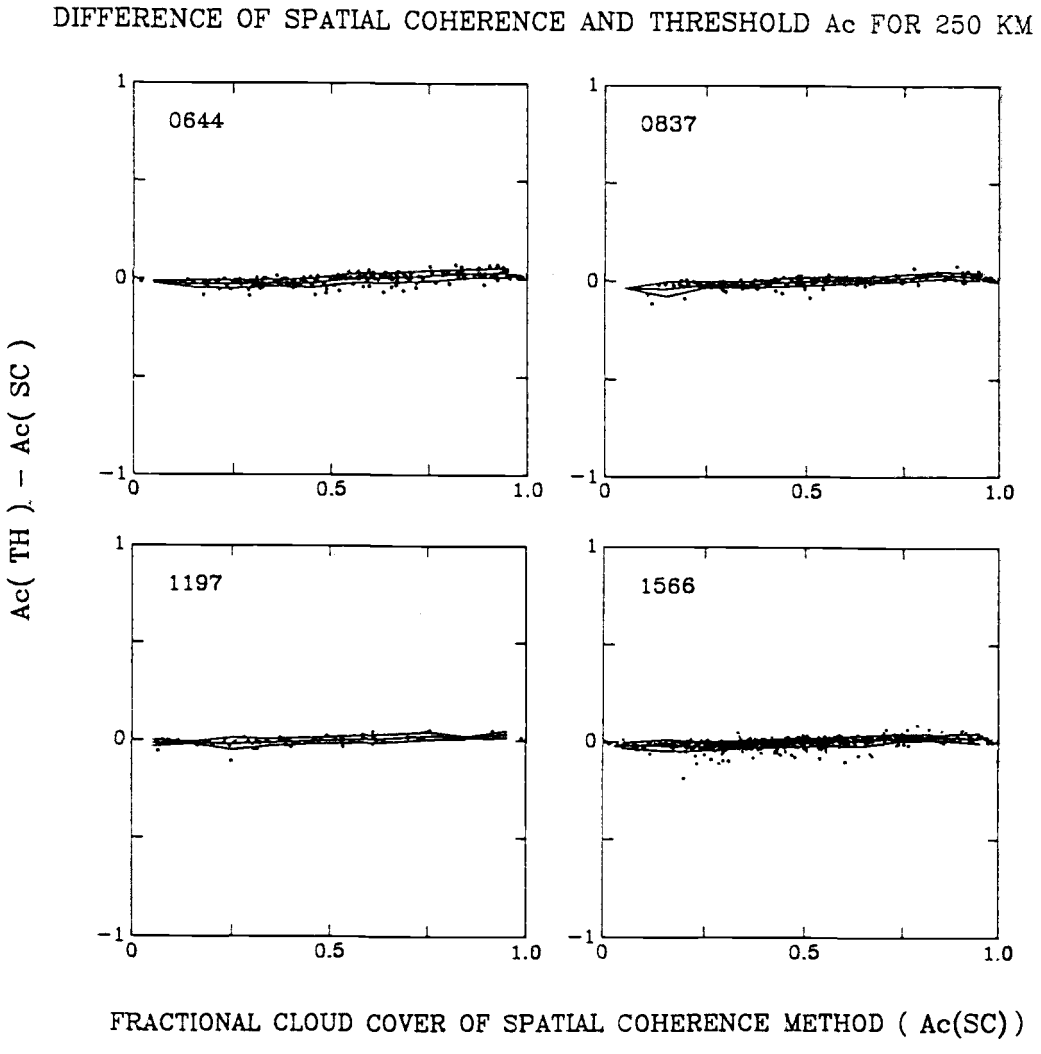

Figure 5.5(b) Differences in cloud cover obtained with the spatial coherence and the midpoint threshold method. Each point is for a frame which at nadir has an area of approximately (250 km)^2.

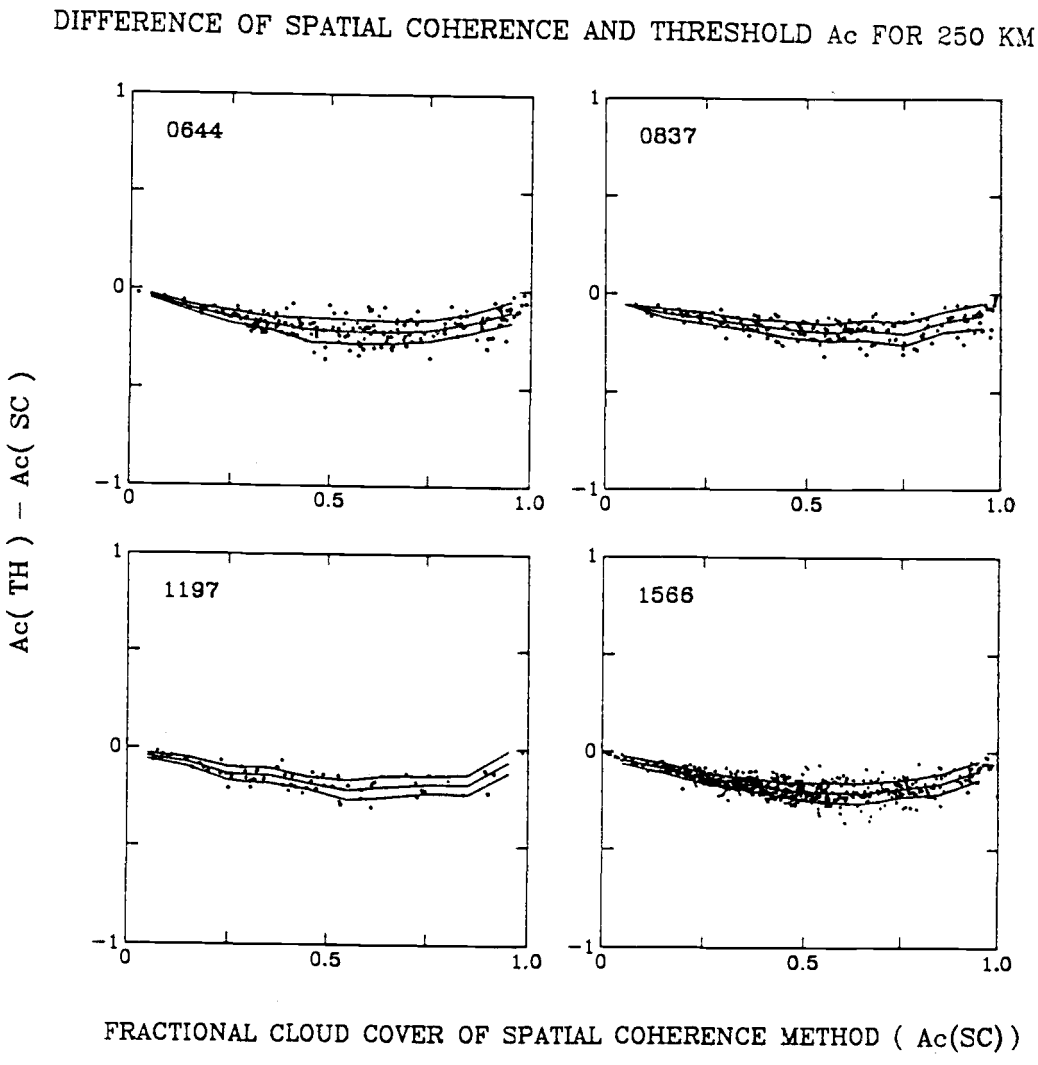

Figure 5.5(c) Differences in cloud cover obtained with the spatial coherence and the overcast threshold method. Each point is for a frame which at nadir has an area of approximately (250 km)^2.

cover of less than 0.5. As a result, the number of pixels for which the cloud-cover fraction is underestimated is larger than the number for which the cloud-cover fraction is overestimated. Aggregating all the pixel-scale cloud-cover fraction leads to an underestimate of the regional cloud-cover fraction. Likewise, for a frame or sub-frame with cloud-cover fraction greater than 0.5, the midpoint threshold will overestimate the frame's or subframe's cloud-cover fraction. Finally, the cloud-cover fractions obtained with the threshold method agreed with those derived by the spatial coherence method when the frames or sub-frames are extensively cloud-free or extensively overcast.

From the above comparisons, it appears that the midpoint threshold gives the best result. Could the midpoint threshold be used to determine the cloud-cover fraction? Provided that both the "true" cloud-free and cloud-covered radiances are known, it might be a good way to determine the cloud-cover fraction. But remember that unless the number of partially covered pixels with cloud-cover fraction less than the midpoint threshold and those with cloud cover greater than the threshold value are equal, which is not often the case, errors will be produced. Furthermore, some method must be used to determine the cloud-covered radiances.

6. Model for Estimating Threshold Errors

It is recognized that errors in fractional cloud cover obtained with threshold methods are due to the presence of partially cloud-covered fields of view. The cloud cover is underestimated when a partially cloud-covered pixel is counted as completely cloud-free and the cloud cover is overestimated when a partially cloud-covered pixel is counted as completely cloud-covered. In order to develop a theoretical model for estimating the errors anticipated from threshold cloud retrieval techniques, it is necessary to know the distribution of fractional cloud cover at the pixel-scale.

Figure 6.1a-d and 6.2a-d show the frequency distributions of fractional cloud-cover at the pixel-scale for (250 km)^2 and (60 km)^2 scales, respectively. These frequency distributions are produced as follows: Within each frame (or sub-frame) which is identified to contain an appropriate single-layered cloud system, a pixel-scale fractional cloud cover is obtained for each pixel by substituting the spatial coherence retrieved clear-sky and cloudy-sky radiances and the observed pixel radiance into (2). Then, in each V-5 region all pixels included in frames (or sub-frames) which contain appropriate single-layered systems are taken and divided into ten groups with respect to their pixel-scale fractional cloud cover. The pixel-scale cloud-cover fractions ranging from 0.0 to 1.0 are divided into ten bins and each bin has a bin size of 0.1. By counting the fraction of pixels within each bin, the frequency distribution of the fractional cloud cover at pixel-scale is computed. The normalization requirement is given by

$$1 = \int_0^1 f(A_c) dA_c \tag{6}$$

where $f(A_c)$ is the frequency of pixel-scale fractional cloud cover between A_c and $A_c + dA_c$. Note that these distributions of pixel-scale cloud cover, as shown in Figure 6.1 and 6.2, are averaged values for several frames (or sub-frames) which have approximately the same cloud cover. For instance, in Figure 6.1(a), the figure with

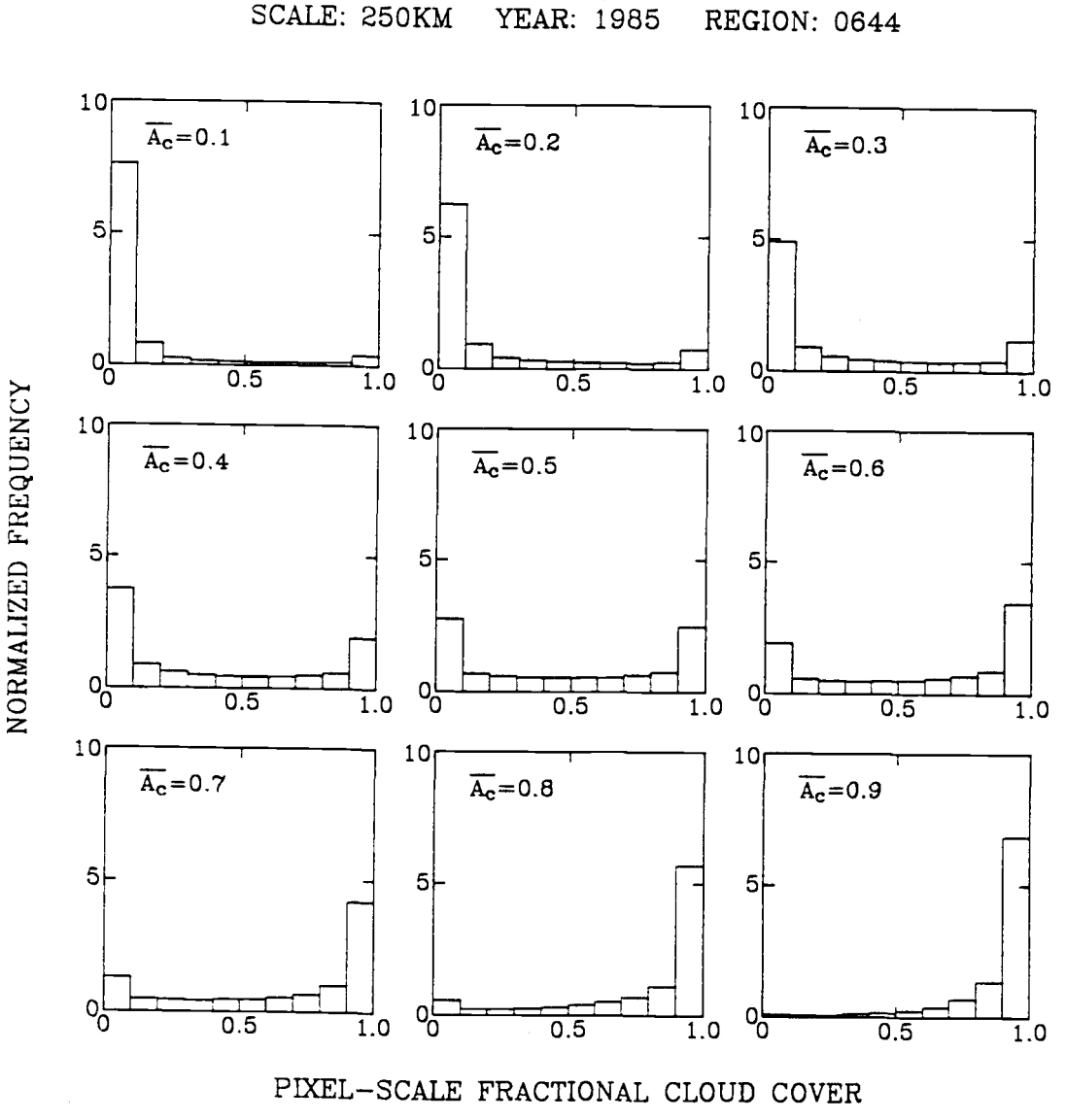

Figure 6.1(a) Observed frequency distribution of pixel-scale cloud cover for region 0644 and for (250 km)^2 frame scale.

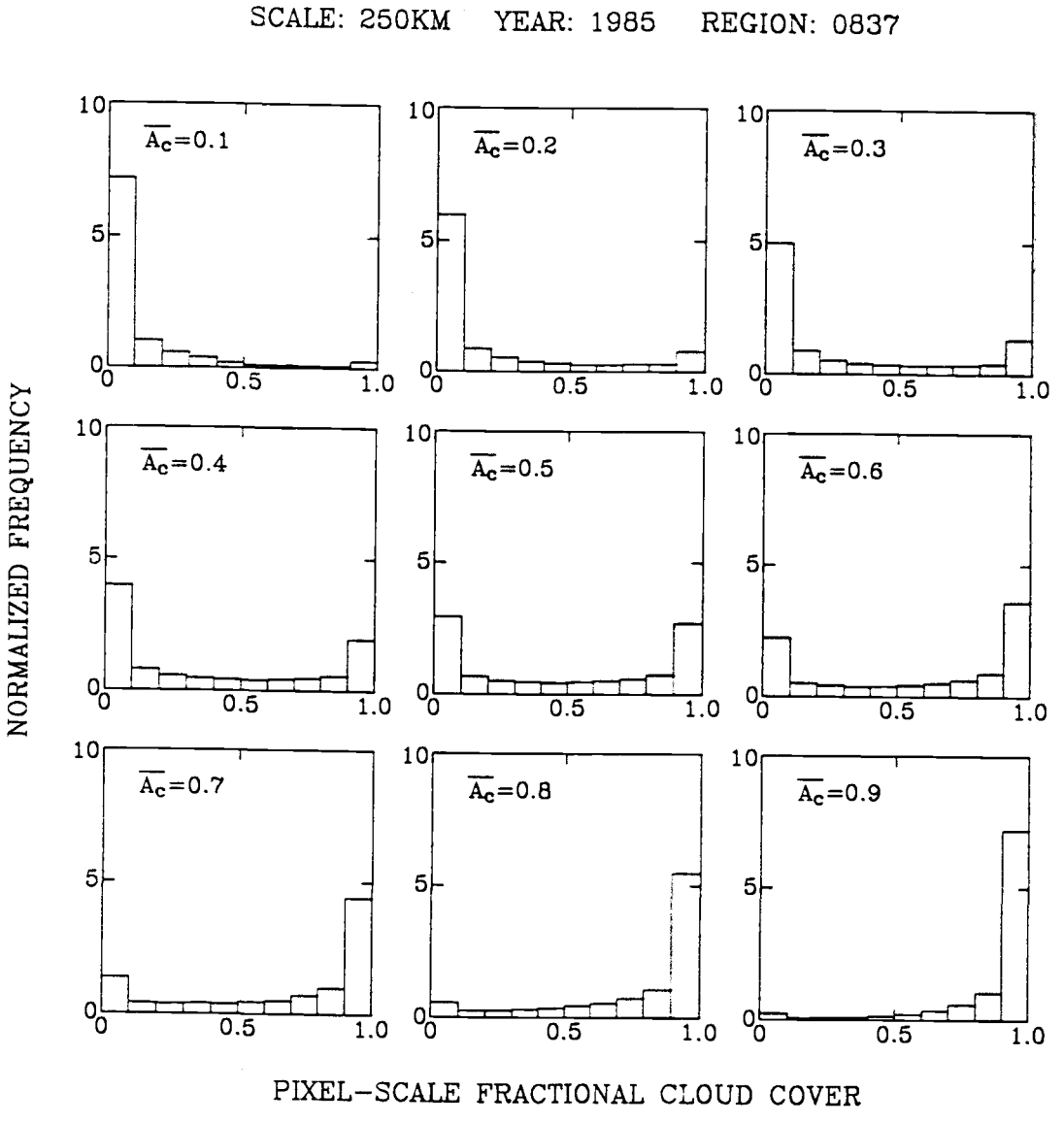

Figure 6.1(b) Observed frequency distribution of pixel-scale cloud cover for region 0837 and for (250 km)^2 frame scale.

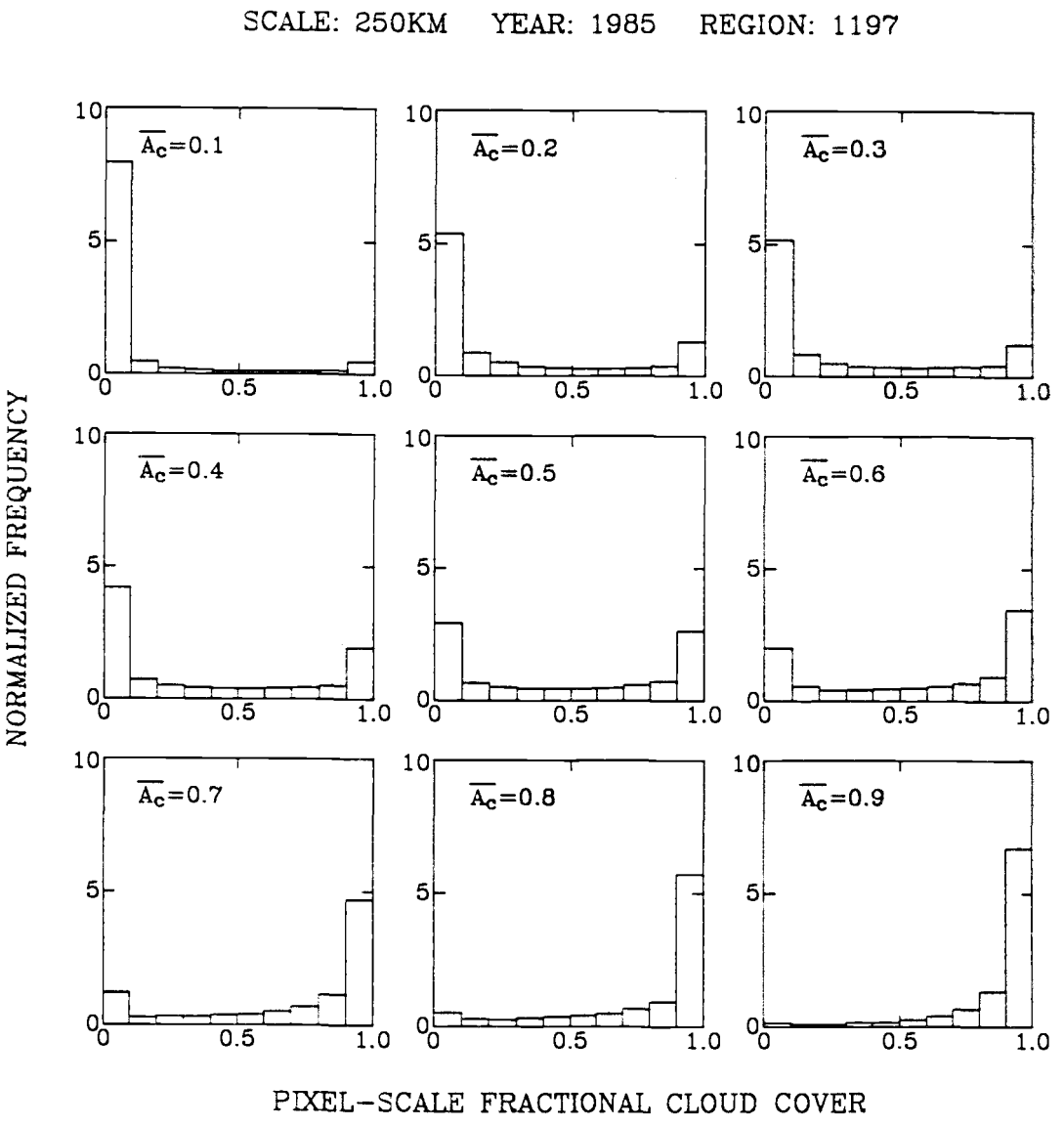

Figure 6.1(c) Observed frequency distribution of pixel-scale cloud cover for region 1197 and for (250 km)^2 frame scale.

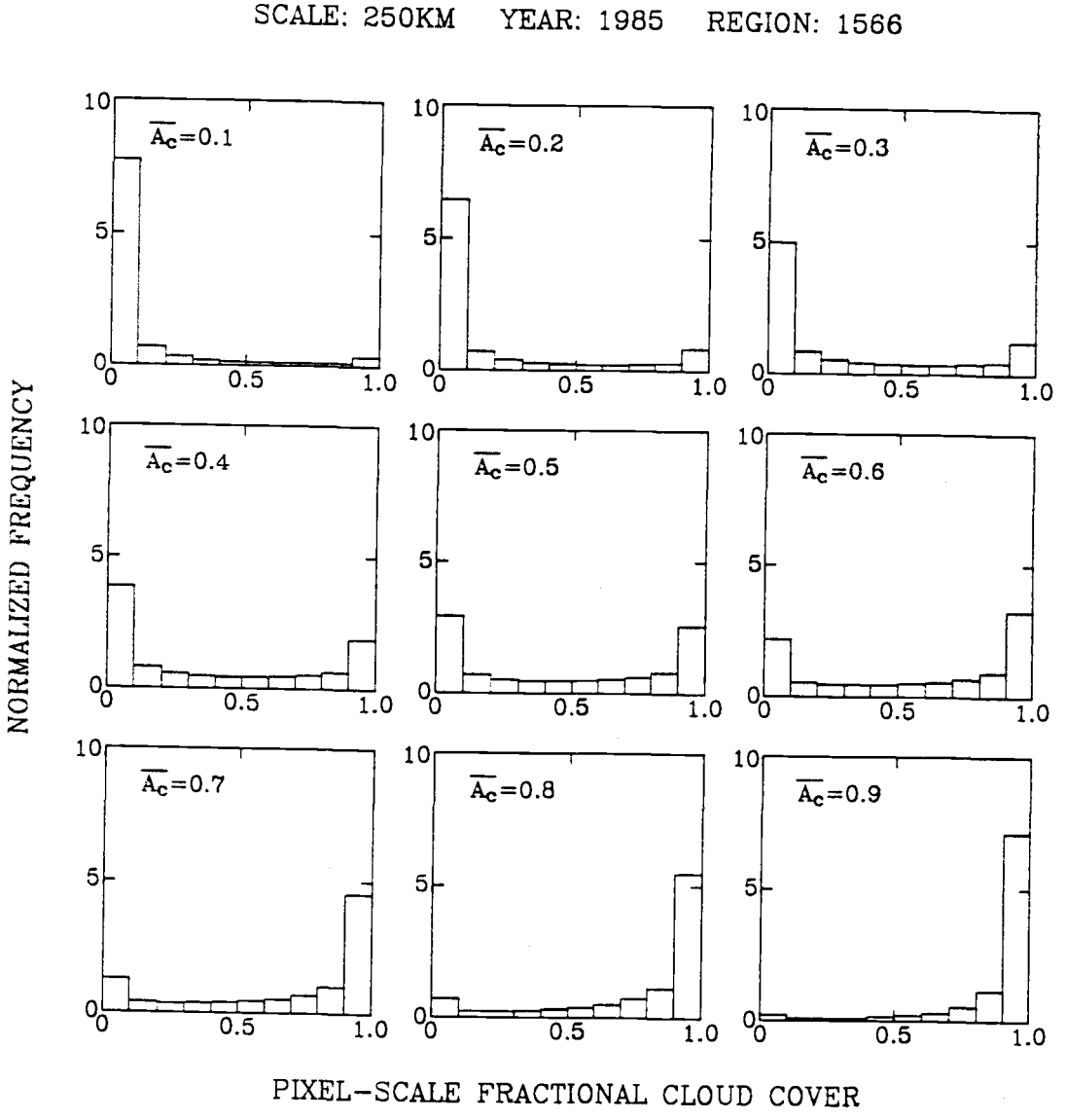

Figure 6.1(d) Observed frequency distribution of pixel-scale cloud cover for region 1566 and for (250 km)^2 frame scale.

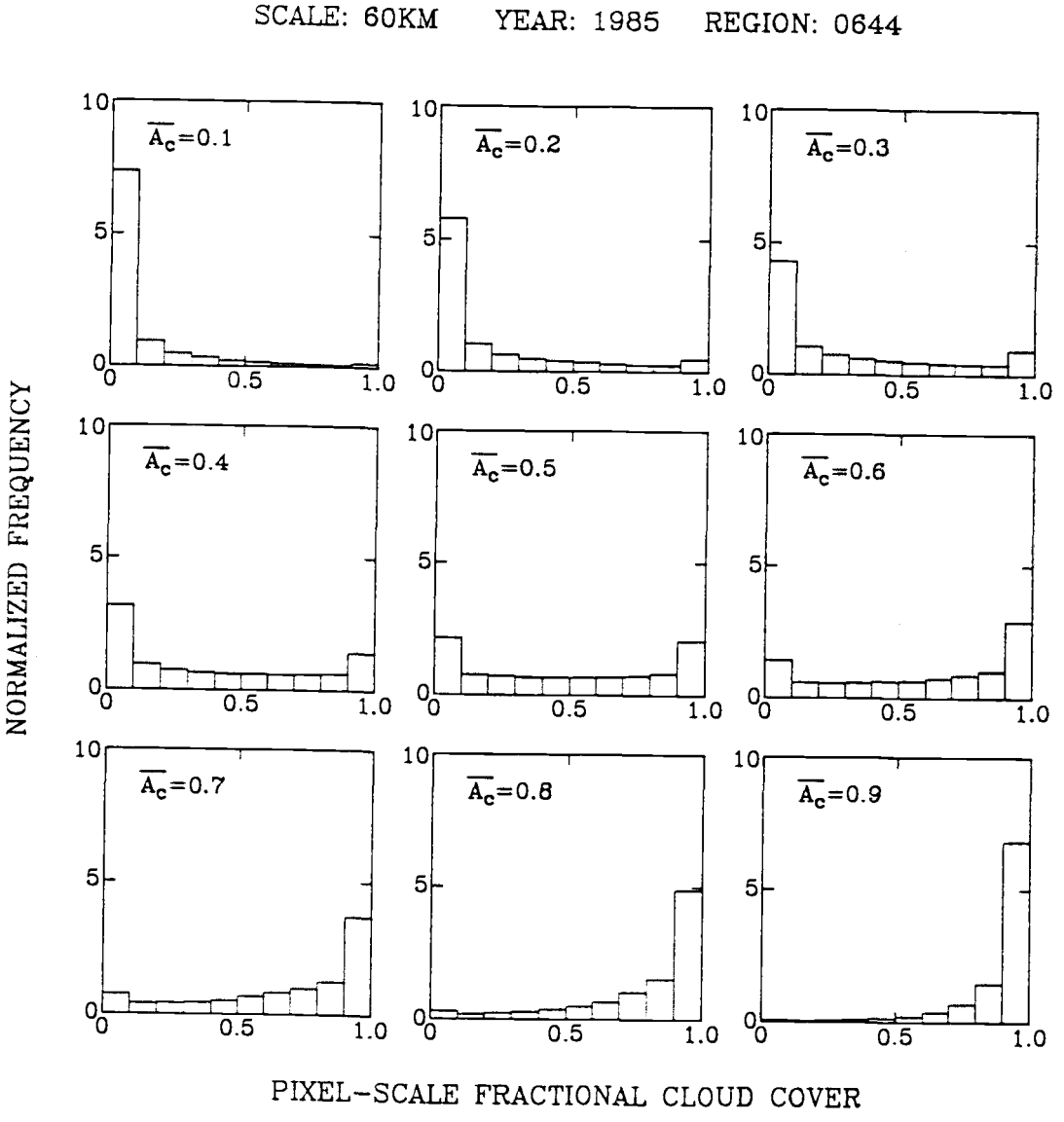

Figure 6.2(a) Observed frequency distribution of pixel-scale cloud cover for region 0644 and for (60 km)^2 subframe scale.

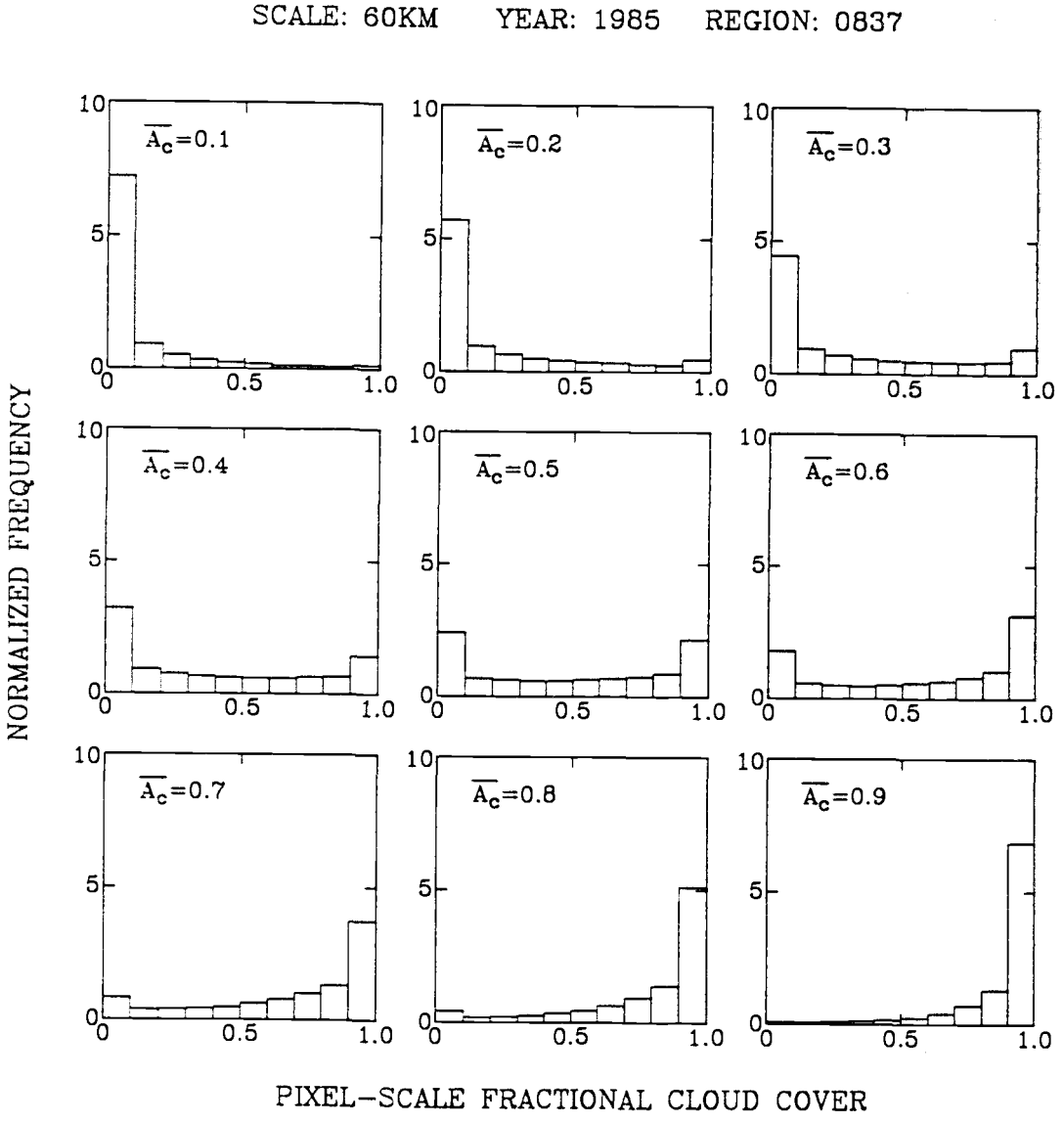

Figure 6.2(b) Observed frequency distribution of pixel-scale cloud cover for region 0837 and for (60 km)^2 subframe scale.

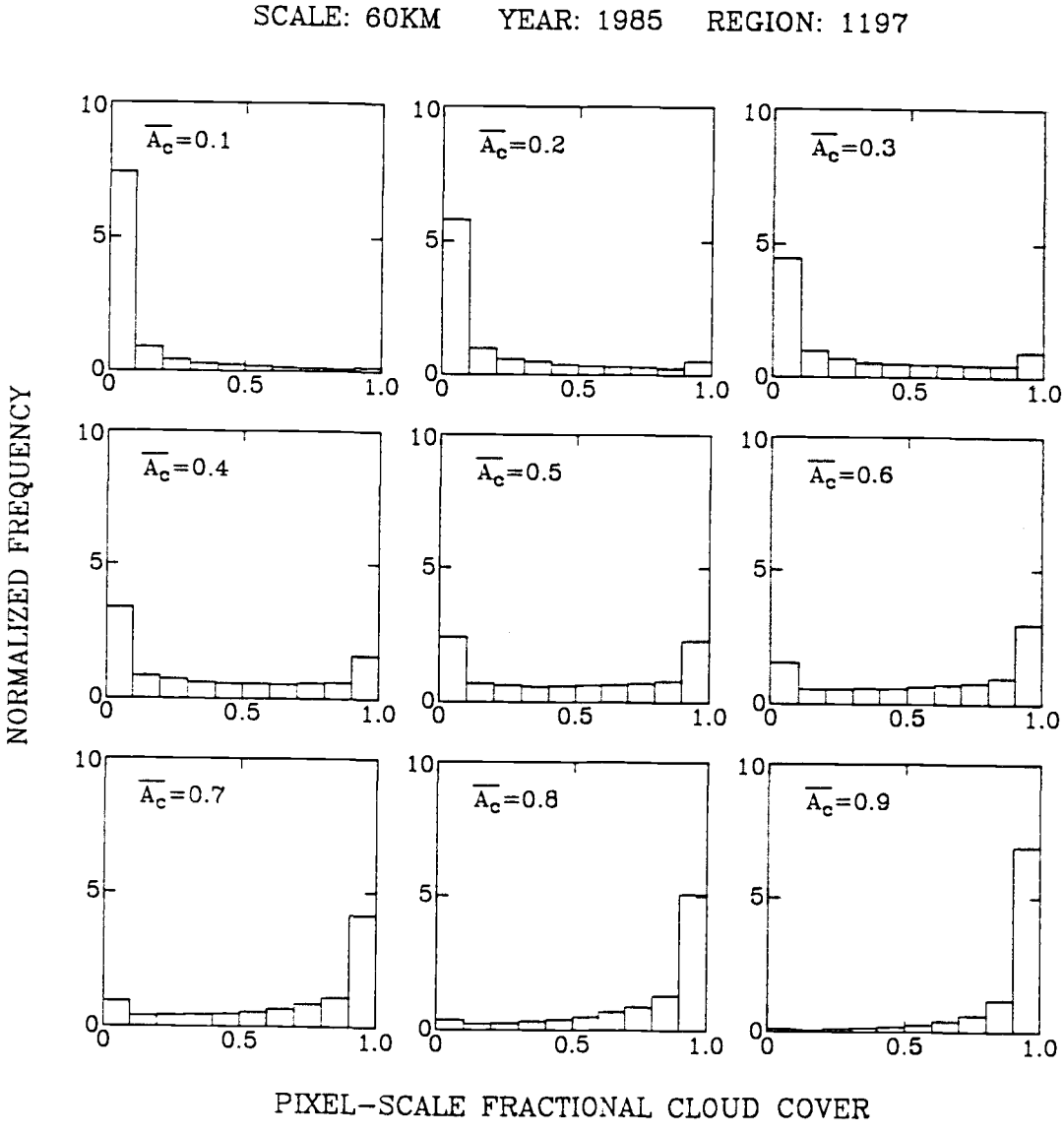

Figure 6.2(c) Observed frequency distribution of pixel-scale cloud cover for region 1197 and for (60 km)^2 subframe scale.

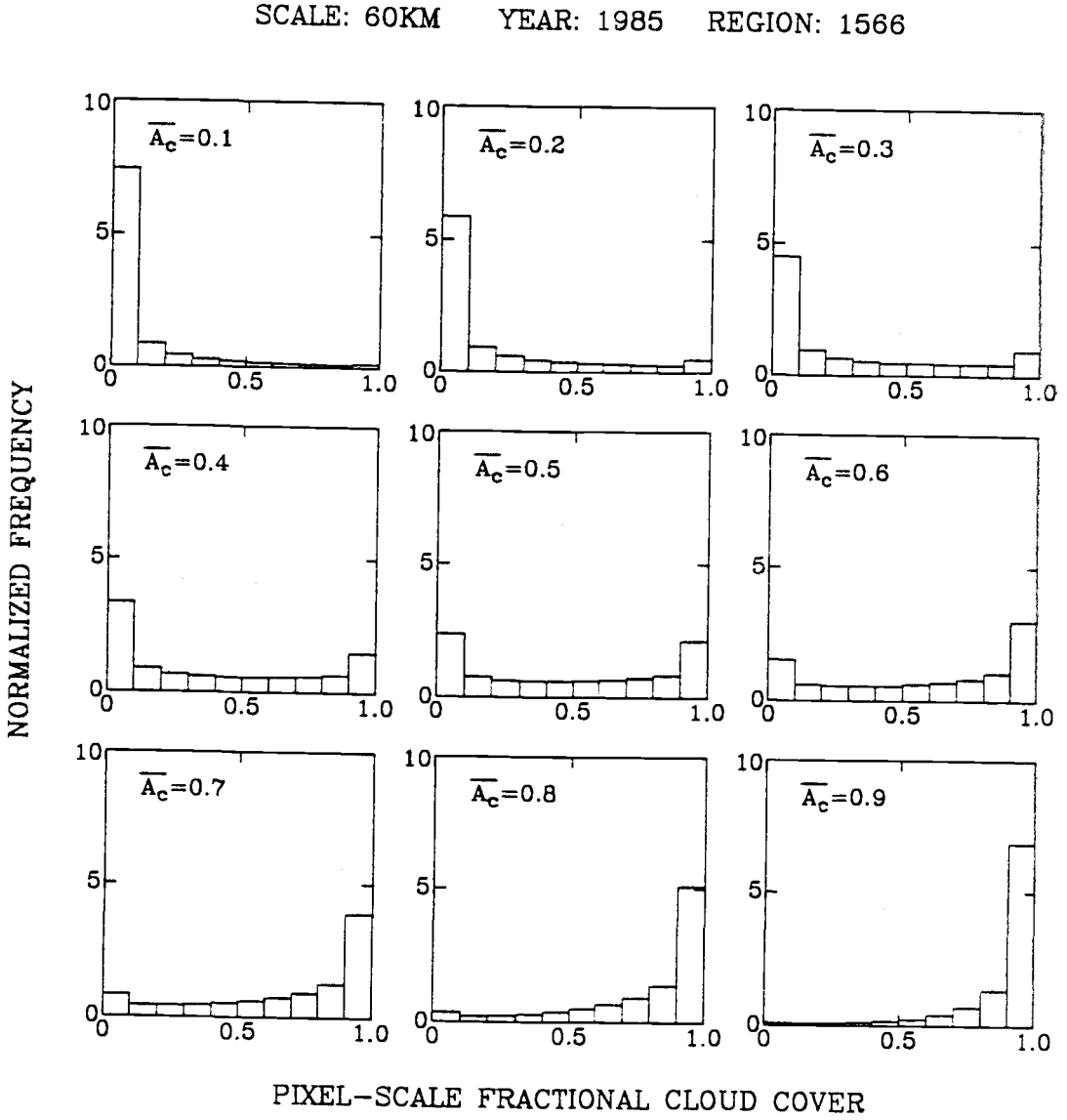

Figure 6.2(d) Observed frequency distribution of pixel-scale cloud cover for region 1566 and for (60 km)^2 subframe scale.

$\overline{A_c} = 0.1$ shows the averaged pixel-scale distribution for frames with $0.05 < \overline{A_c} < 0.15$. The averaged fractional cloud cover for a collection of pixels is given by

$$\overline{A_c} = \int_0^1 f(A_c) A_c dA_c \,. \tag{7}$$

In Figure 6.3(a) and (b), frequency distributions of cloud cover at the frame scale and at the sub-frame scale are shown, respectively. Evidently, for single-layered cloud systems a large fraction of (4 km)^2 pixels contain broken clouds. The percentages of partially cloud-covered pixels for a region can be estimated from the distribution of frame-scale or subframe-scale cloud cover (Figure 6.3) and the distribution of pixel-scale cloud cover (Figure 6.1 and 6.2). Table 2 shows the percentages of partially cloud-covered pixels obtained for four V-5 regions and for both (250 km)^2 and (60 km)^2 scales. As shown in Table 2, the percentages of partially cloud-covered pixels are, as they should be, approximately the same for both (250 km)^2 and (60 km)^2 scales. Approximately half the pixels included in the four V-5 regions contain broken clouds. In fact, most clouds neither avoid nor completely fill the satellite instrument's field of view ($\sim$1–8 km).

By comparing Figure 6.1 and 6.2, the frequency distributions for pixel-scale fractional cloud cover on the frame scale and sub-frame scale appear to be different. The primary difference is that the fractions of partially covered pixels for the sub-frame scale are larger than those for the frame scale. The reason that the distributions appear different is because of the different ways that clouds populate (250 km)^2 and (60 km)^2

Table 2 Percentages of partially cloud-covered pixels

(%)	0644	0837	1197	1566
(250 km)	50.4	46.5	48.3	50.8
(60 km)	49.7	46.3	51.2	52.2

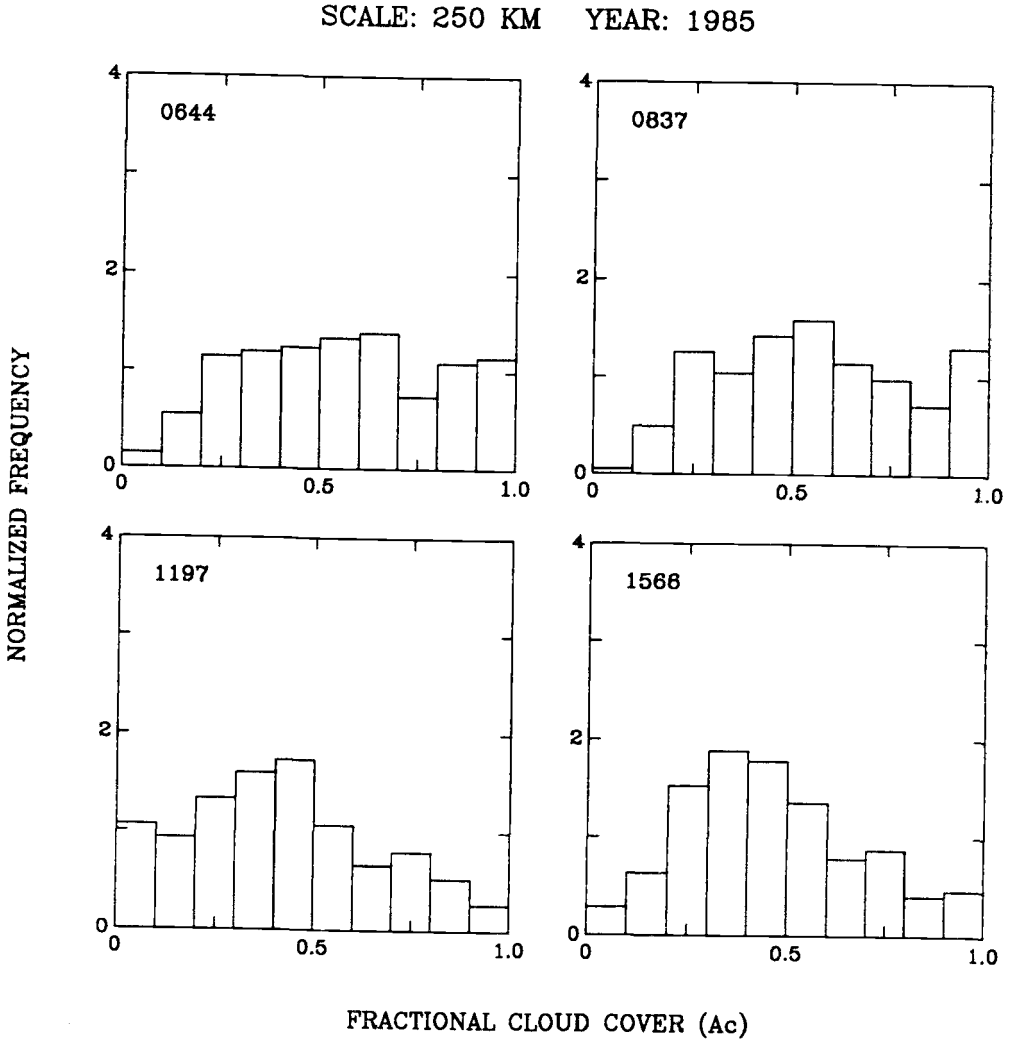

Figure 6.3(a) Observed frequency distribution of cloud cover for (250 km)^2 regions.

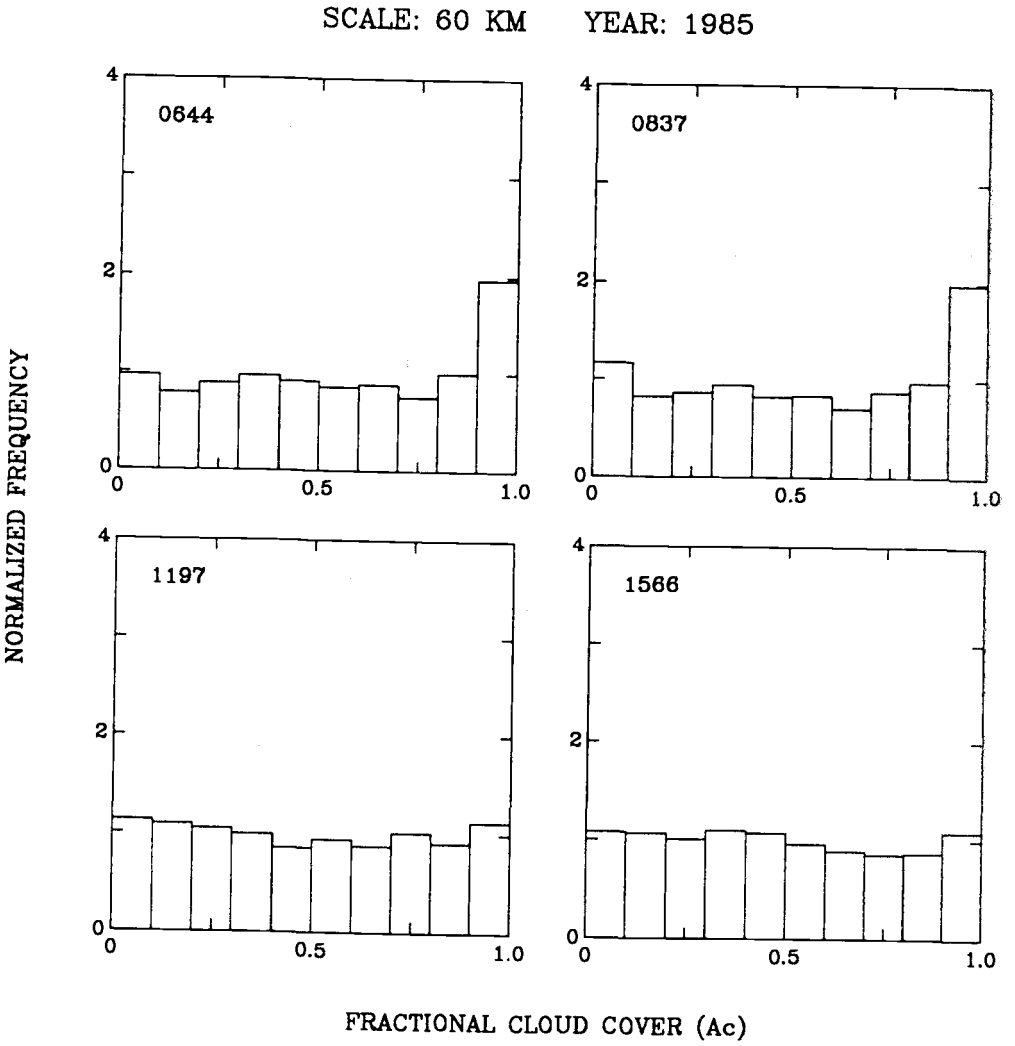

Figure 6.3(b) Observed frequency distribution of cloud cover for (60 km)^2 regions.

regions. For example, assume a (250 km)^2 region and a (60 km)^2 region have the same cloud-cover fraction of 0.5. Three types of pixels, cloud-free, partially cloud-covered, and overcast, populate both regions. Based on Figure 6.3 it is more likely that a (60 km)^2 region will be either overcast or cloud-free than a (250 km)^2 region. It seems reasonable, therefore, to expect that on occasion a (250 km)^2 region will achieve a cloud cover of 0.5 by having large sub-areas that are either overcast or cloud-free so that the fraction of partially covered pixels need not be large. On the other hand, for a (60 km)^2 region, the large fractions of partially covered pixels appear when the region is partially covered.

The distribution of the fractional cloud cover at the pixel-scale, as shown in these figures, appears to be stable from one region to the next. The number of cloud-free pixels decreases and the number of overcast pixels increases while the cloud cover in the frame or sub-frame increases. The fraction of partially covered pixels approaches a maximum when the cloud-cover fraction in the frame or sub-frame approaches ~0.5. The fraction of partially covered pixels decreases while the cloud-cover fraction in the frame or sub-frame either increases to one or decreases to zero.

To estimate the errors in fractional cloud cover obtained with the threshold method, it is assumed that the regional errors, such as (250 km)^2, (60 km)^2, etc., are accumulations of the errors made in each of the pixels. The threshold error is then given by

$$\varepsilon = \int_0^{A_{cth}} \epsilon(A_c) f(A_c) dA_c + \int_{A_{cth}}^1 \epsilon(A_c) f(A_c) dA_c \tag{8}$$

where $\epsilon(A_c)$ is the error in a pixel and ε is the regional error. For each pixel the error due to the application of a threshold is given by

$$\epsilon(A_c) = -A_c \tag{9}$$

when $A_c < A_{cth}$

$$\epsilon(A_c) = 1 - A_c \tag{10}$$

when $A_c > A_{cth}$, where A_c is the fractional cloud cover in the pixel and A_{cth} is the fractional cloud cover associated with the threshold value of the radiance that determines a pixel to be cloud-free or overcast. Thus, the regional error due to the application of a threshold is given by

$$\varepsilon = -\int_0^{A_{cth}} A_c f(A_c) dA_c + \int_{A_{cth}}^1 (1 - A_c) f(A_c) dA_c \,. \tag{11}$$

While $f(A_c)$ and its dependence on regional-scale cloud cover are shown in the previous figures, errors in the fractional cloud cover obtained with a threshold method are readily predicted by assuming simple approximations for such distributions.

Figure 6.4 illustrates the simplest representation for the distribution of pixel-scale fractional cloud cover. The partially covered pixels are assumed to populate a uniform frequency distribution. Thus, due to the normalization requirement, a is

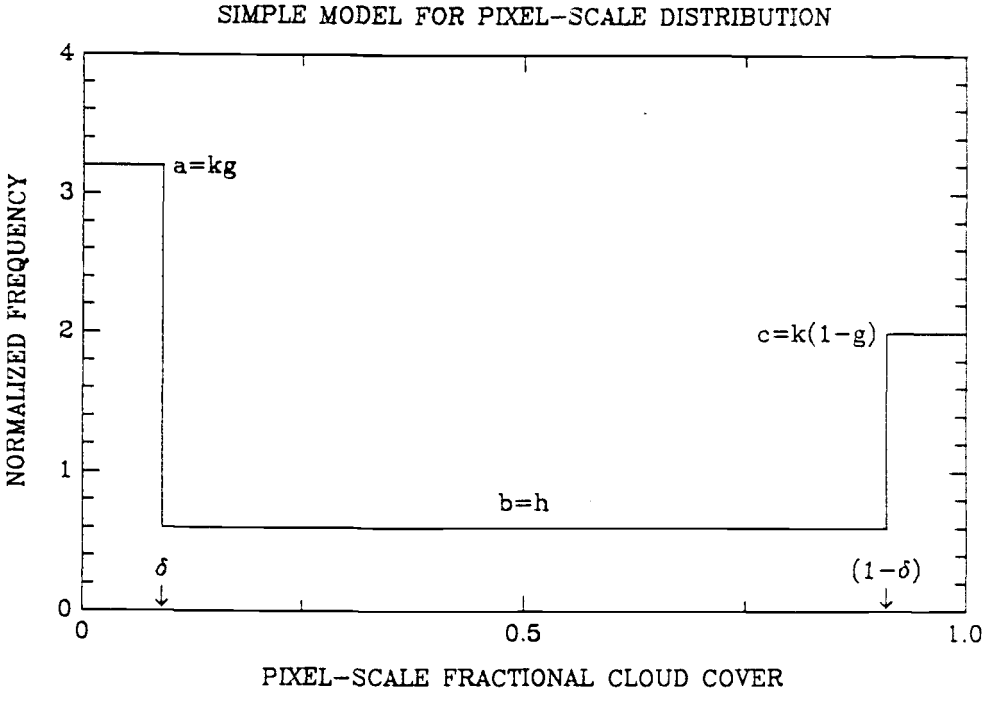

Figure 6.4 Simple model for frequency distribution of pixel-scale cloud cover.

related to c by

$$a = kg \tag{12}$$

and

$$c = k(1 - g) \tag{13}$$

where k is some constant and $0 \leq g \leq 1$. If b is set to h, then for $\delta = 0.1$ (as shown in Figure 6.4) a and c are given by

$$a = (10 - 8h)g \tag{14}$$

and

$$c = (10 - 8h)(1 - g) \tag{15}$$

In the above analysis the fractional cloud cover is set to zero for pixels with $A_c < \delta$, which are said to be cloud-free, and it is set to one for pixels with $A_c > 1 - \delta$, which are said to be overcast. In practice, the values used for δ are not critical. Reasonable values are $0.05 \leq \delta \leq 0.2$. Changing δ will, of course, alter the expressions for a and c in accordance to the normalization conditions, but the changes will have little effect on the estimates of cloud-cover errors and no effect on major conclusions. Using the above representation for the distribution in (11), the error due to the application of a threshold is given by

$$\varepsilon = (0.5 - A_{cth})h \tag{16}$$

It is assumed that there is no error for cloud-free pixels, $A_c < \delta$, and again no error for overcast pixels, $A_c > 1 - \delta$.

According to (16), once the threshold, A_{cth}, is determined, the error, ε, depends only on h which in turn is proportional to the number of partially cloud-covered pixels. The error does not depend on the balance between overcast pixels, $A_c < \delta$, and cloud-free pixels, $A_c > 1 - \delta$, as are given by g in (12) and (13), because these

pixels contribute no error to the cloud-cover fraction. Also, in this idealized model the threshold error is minimal and equals zero when the radiance associated with the threshold is set at $A_{cth} = 0.5$. Furthermore, ε is symmetric in $A_{cth} = 0.5$. That is, setting the threshold at a radiance for which $A_{cth} < 0.5$ produces a positive error representing a systematic overestimate of cloud-cover fraction and setting the threshold at a radiance for which $A_{cth} > 0.5$ produces a negative error representing a systematic underestimate of cloud-cover fraction. Figure 6.5 shows the values of h obtained for (250 km)^2 and (60 km)^2 scales over four regions. These values are calculated by averaging the frequency distribution of partially covered pixels, as shown in Figure 6.1 and 6.2. The averaged frequency is obtained for each of the distributions which have different mean regional-scale cloud cover, $\overline{A_c}$.

Because the values of h are approximately symmetric in $\overline{A_c}$ and $(1 - \overline{A_c})$, we

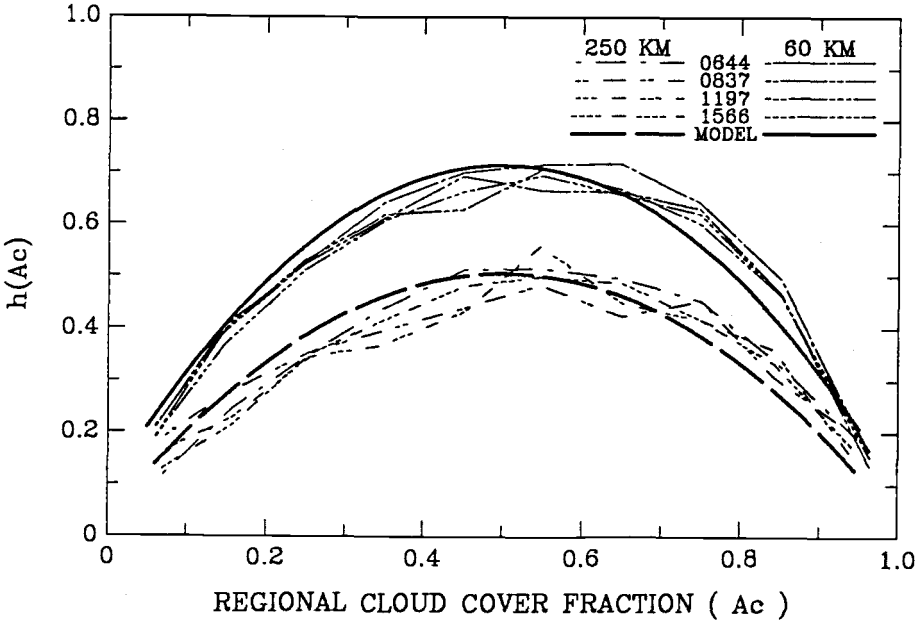

Figure 6.5 Average frequency of partially covered pixels, h, as a function of regional scale cloud cover. Results for both (250 km)^2 frames and (60 km)^2 subframes are shown.

take h to be given by

$$h = 0.03 + 1.90\overline{A_c}(1 - \overline{A_c}) \tag{17}$$

for (250 km)^2 scale and

$$h = 0.09 + 2.50\overline{A_c}(1 - \overline{A_c}) \tag{18}$$

for (60 km)^2 scale. With these fits, threshold errors associated with a particular A_{cth} can be easily estimated using (16).

To illustrate the estimates of threshold errors, three different thresholds, as described in section 2, are used in the simple model. The fractional cloud cover, A_{cth}, corresponding to each threshold is taken to be the mean value obtained for the ensemble of cases. The associated values are 1) the cloud-free threshold: $A_{cth} = 0.15$, 2) the midpoint threshold: $A_{cth} = 0.50$, and 3) the overcast threshold: $A_{cth} = 0.85$. Figure 6.6 shows the mean differences between the threshold and the spatial coherence methods derived cloud-cover fractions for the three different thresholds applied to the four regions. The errors estimated by (16) are also plotted and compared with the mean differences that were shown in Figure 5.4 and 5.5. These mean differences are plotted as a function of the spatial coherence regional cloud-cover fraction and are calculated by dividing the regional cloud-cover fraction into 10 bins of 0.1 and then averaging the points that fall within each bin. The model estimated errors are zero when $A_{cth} = 0.50$. With these mean cloud-cover-fraction equivalent thresholds, A_{cth}, the mean differences in cloud-cover fraction predicted by (16) are close to those observed.

The standard deviation of estimated error can be derived from (11) and is given by

$$\Delta\varepsilon = (0.5 - A_{cth})\Delta h \tag{19}$$

Figure 6.7 shows that the standard deviation, Δh, associated with the h shown in Figure 6.5. These values of Δh are calculated from the frequency distribution of pixels with cloud-cover fraction between δ and $1 - \delta$ while the mean value is as

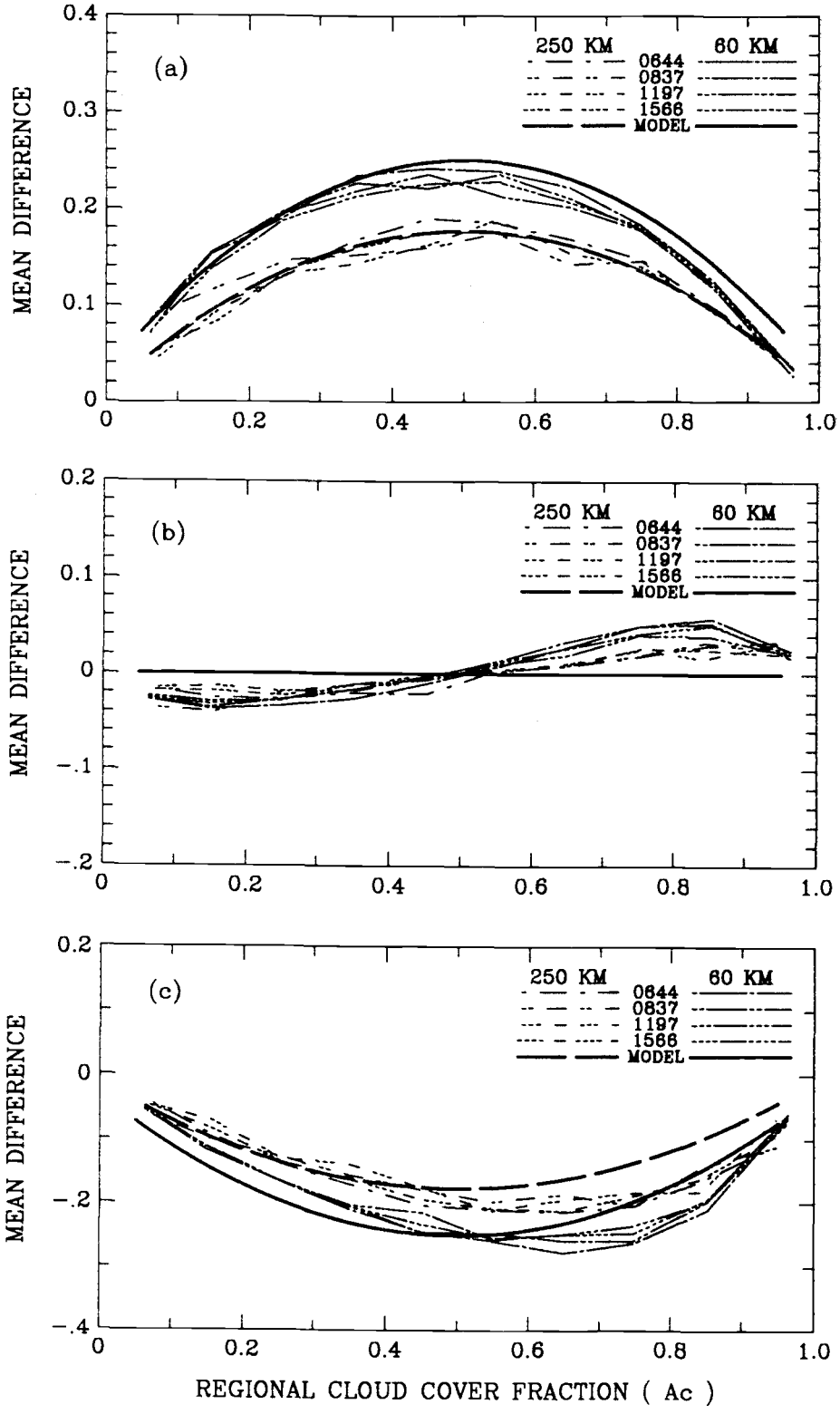

Figure 6.6 Mean differences in cloud cover (threshold – spatial coherence) for V-5 regions and that predicted by 1-parameter model. (a), (b), and (c) are respectively for the cloud-free threshold, midpoint threshold, and overcast threshold.

described above. Since Δh is roughly symmetric in $\overline{A_c}$ and $(1-\overline{A_c})$, as shown in Figure 6.7, the fits of Δh are taken to be given by

$$\Delta h = 0.05 + 0.30\overline{A_c}(1-\overline{A_c}) \tag{20}$$

for $(250\text{km})^2$ scale and

$$\Delta h = 0.11 + 0.40\overline{A_c}(1-\overline{A_c}) \tag{21}$$

for $(60\text{km})^2$ scale. With these fits for Δh, the standard deviations of predicted errors can be estimated. Figure 6.8 shows the standard deviations obtained using (19) and the errors shown in Figures 5.4 and 5.5. Again, the estimated errors are zero for $A_{cth} = 0.5$. The estimates of $\Delta\varepsilon$ describe the random uncertainty in threshold derived cloud cover. They give the spread of the points shown in Figures 5.4 and 5.5.

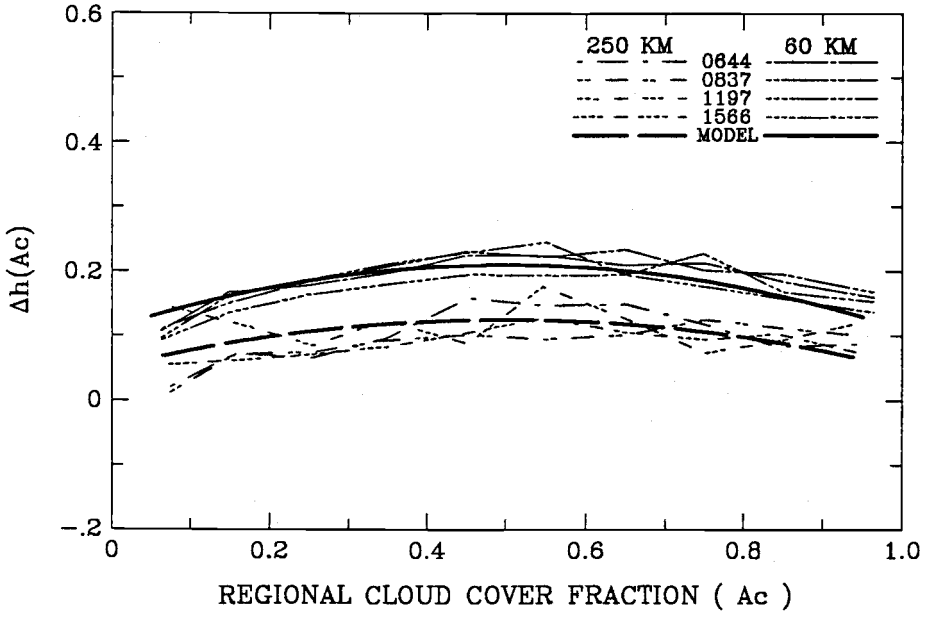

Figure 6.7 Δh as a function of regional scale cloud cover. Results for both $(250\text{ km})^2$ frames and $(60\text{ km})^2$ subframes are shown.

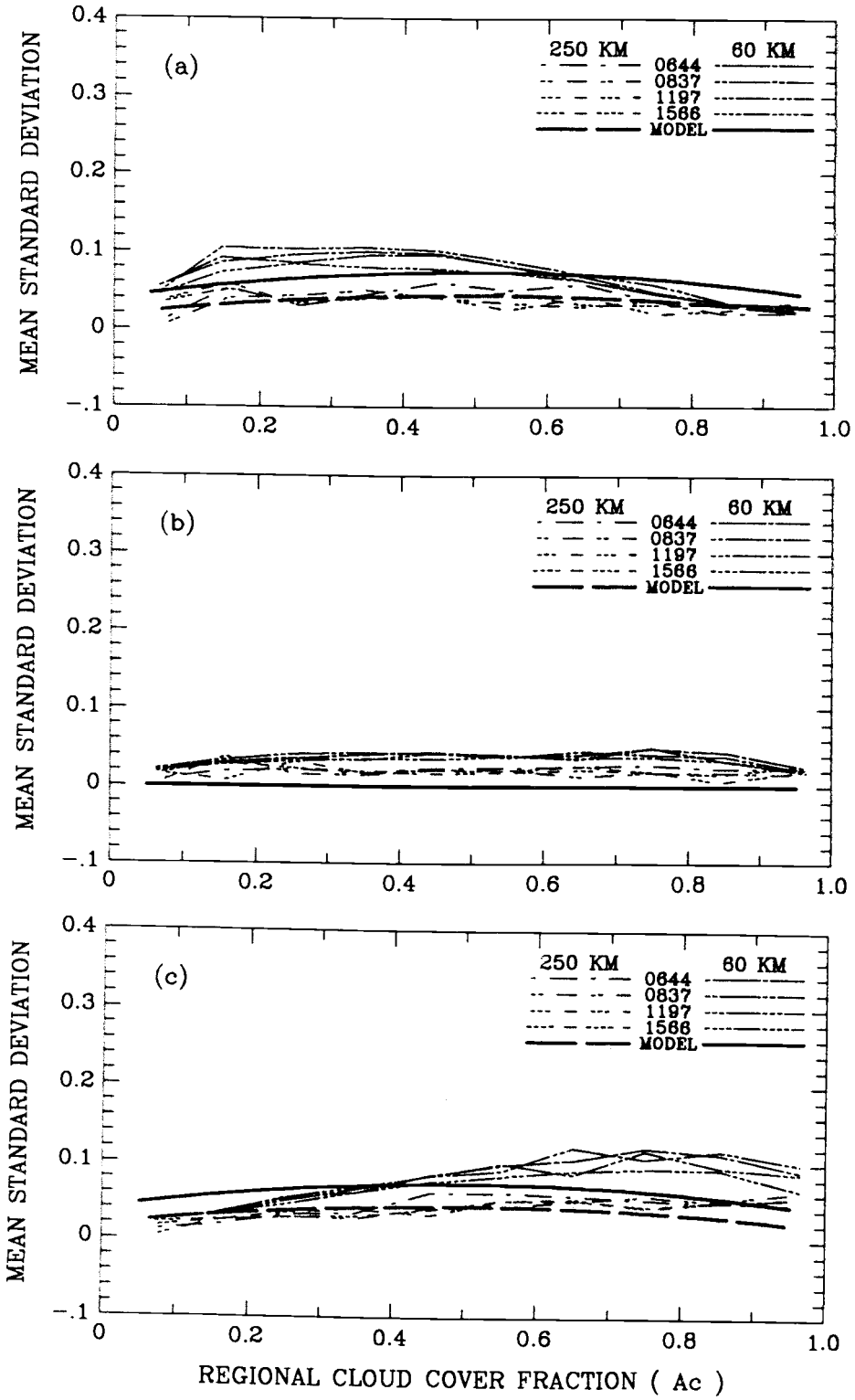

Figure 6.8 Standard deviations of mean differences in cloud cover for V-5 regions and that predicted by 1-parameter model. (a), (b), and (c) are respectively for the cloud-free threshold, midpoint threshold, and overcast threshold.

7. Improved Model for Estimating Threshold Errors

As shown in Figures 6.1 and 6.2, the distribution of pixel-scale fractional cloud cover is a function of the regional-scale cloud cover. When the regional-scale cloud cover is small, the partially covered pixels within the region also generally contain small cloud cover. Similarly, when the regional-scale cloud cover is large, the pixels with broken clouds generally contain large cloud cover. Since the simple model with one value for the frequency of all partially-covered pixels fails to capture these trends, there are noticeable errors in the predicted differences between spatial coherence and threshold derived cloud-cover fractions. An improved model for fitting the distribution of partially-covered pixels is obtained by adding another parameter to account for the trends in the frequency of occurrence for the partially-covered pixels.

Figure 7.1 illustrates a two-parameter model for the distribution of pixel-scale

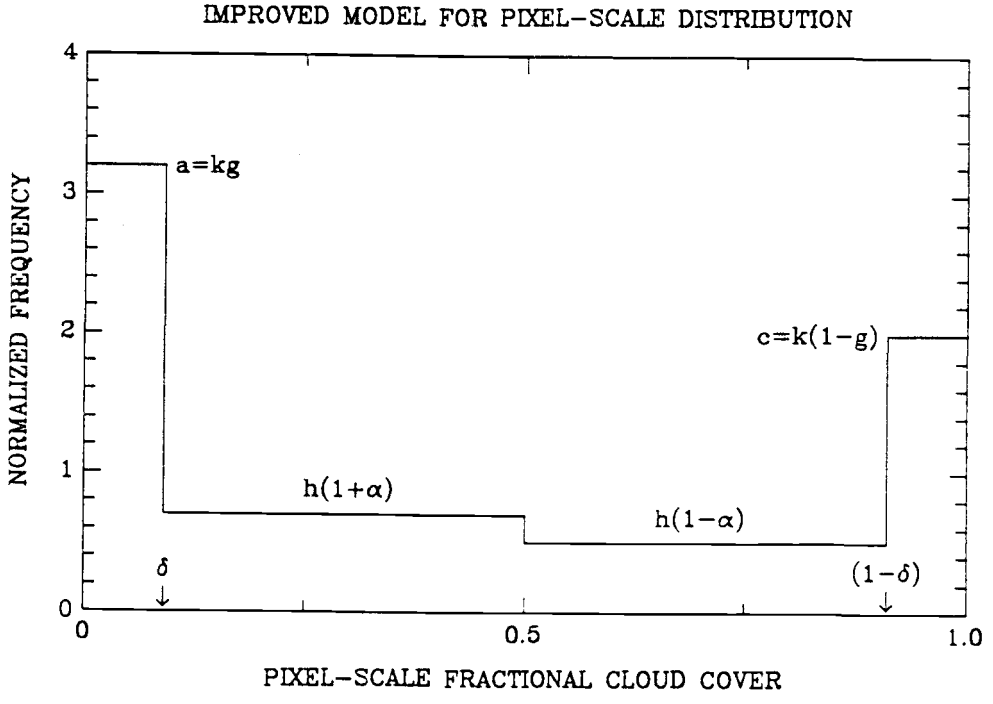

Figure 7.1 2-parameter model for frequency distribution of pixel-scale cloud cover.

fractional cloud cover. As shown in the figure, the distribution of the partially covered pixels is given by

$$h(1+\alpha) \tag{22}$$

for pixels with fractional cloud cover, $A_c < 0.5$ and

$$h(1-\alpha) \tag{23}$$

for pixels with fractional cloud cover, $A_c > 0.5$, where $-1 < \alpha < 1$. Thus, the new parameter, α, characterizes the difference between the pixel-scale frequency distribution of pixels with fractional cloud cover less than 0.5 and that of pixels with fractional cloud cover greater than 0.5. Since

$$\frac{[h(1+\alpha)+h(1-\alpha)]}{2} = h \tag{24}$$

the pixel-scale frequency distribution of the improved 2–parameter model has the same amount of partially-covered pixels as that of the simple model.

Again, with this improved 2–parameter model, the expression for the estimates of threshold error can be derived from (11). The error is given by

$$\varepsilon = h(0.5 - A_{cth}) + \alpha h\left(|0.5 - A_{cth}| - 0.25 + \delta^2\right) \tag{25}$$

and the standard deviation associated with this error is given by

$$\Delta\varepsilon = \Delta h(0.5 - A_{cth}) + \Delta(\alpha h)\left(|0.5 - A_{cth}| - 0.25 + \delta^2\right) \tag{26}$$

where α is again determined by the difference between the mean frequency of pixels with fractional cloud cover from δ to 0.5 and the mean frequency of pixels with fractional cloud cover from 0.5 to $1 - \delta$. Figure 7.2 shows the observed values of α obtained from Figures 6.1a-d and 6.2a-d for (250 km)^2 and (60 km)^2 scales, respectively. The curves in these figures appear to be proportional to $0.5 - A_c$. Fits for observed values of α are also plotted in the figures. The fits are given by

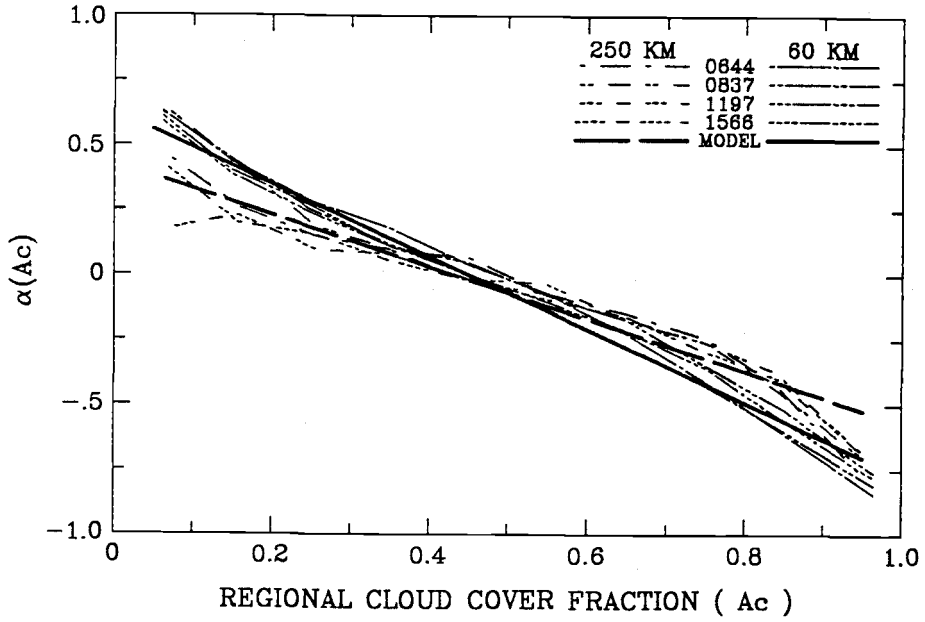

Figure 7.2 α as a function of regional scale cloud cover. Results for both (250 km)^2 frames and (60 km)^2 subframes are shown as a function of regional scale cloud cover.

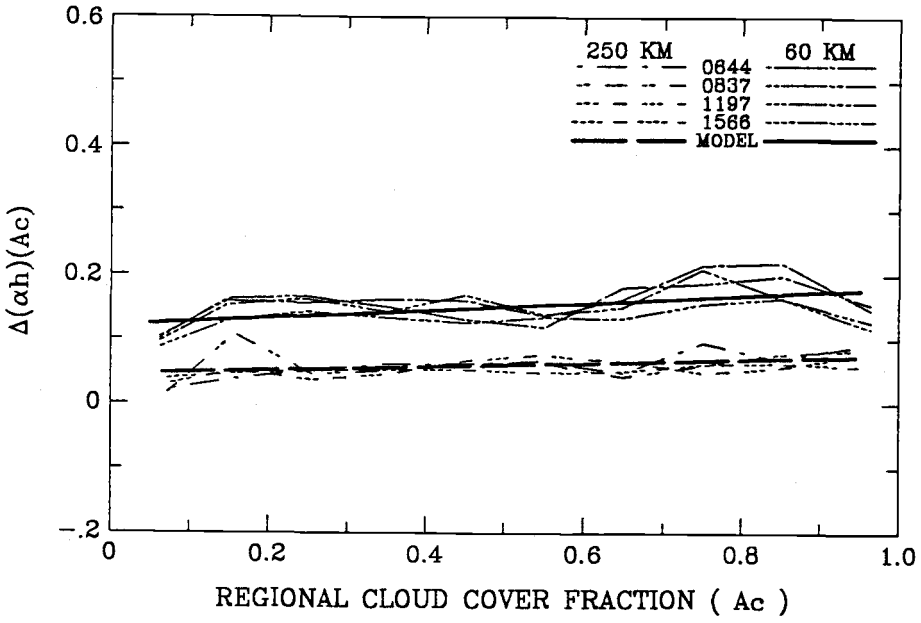

Figure 7.3 $\Delta(\alpha h)$ as a function of regional scale cloud cover. Results for both (250 km)^2 frames and (60 km)^2 subframes are shown as a function of regional scale cloud cover.

$$\alpha = -0.07 + 1.0(0.5 - A_c) \tag{27}$$

for (250km) scale and

$$\alpha = -0.07 + 1.4(0.5 - A_c) \tag{28}$$

for (60km) scale.

For convenience, $\Delta(\alpha h)$ is regarded as a single variable. The calculated values and fits of $\Delta(\alpha h)$ are shown in Figure 7.3. The fits of $\Delta(\alpha h)$ are taken to be given by

$$\Delta(\alpha h) = 0.06 - 0.03(0.5 - A_c) \tag{29}$$

for (250 km)^2 scale and

$$\Delta(\alpha h) = 0.15 - 0.06(0.5 - A_c) \tag{30}$$

for (60 km)^2 scale. With these fits for h, α, Δh, and $\Delta(\alpha h)$, the mean difference, ε, and standard deviation, $\Delta\varepsilon$, can be estimated using (25) and (26). The mean difference and standard deviation estimated by the improved model are, respectively, shown in Figures 7.4 and 7.5 for the three thresholds, $I_s - 3\Delta I_s$, $(I_s + I_c)/2$, and $I_c + 3\Delta I_c$. The errors and standard deviations that are shown in Figures 5.4 and 5.5 are also plotted for comparisons. Comparing Figures 7.4 and 7.5 with Figures 6.5 and 6.7, respectively, the largest improvement is for $A_{cth} = 0.5$. The estimates of the standard deviation within all the figures associated with the improved model also appear to have some improvement. In the case of $A_{cth} = 0.5$, the estimated standard deviations are no longer zero as in the simple model. Clearly, a more representative model for the frequency distribution of pixel-scale fractional cloud cover would probably provide better estimates of errors for threshold methods, but the results of the 1–parameter and 2–parameter models presented in this study appear to be reasonably good.

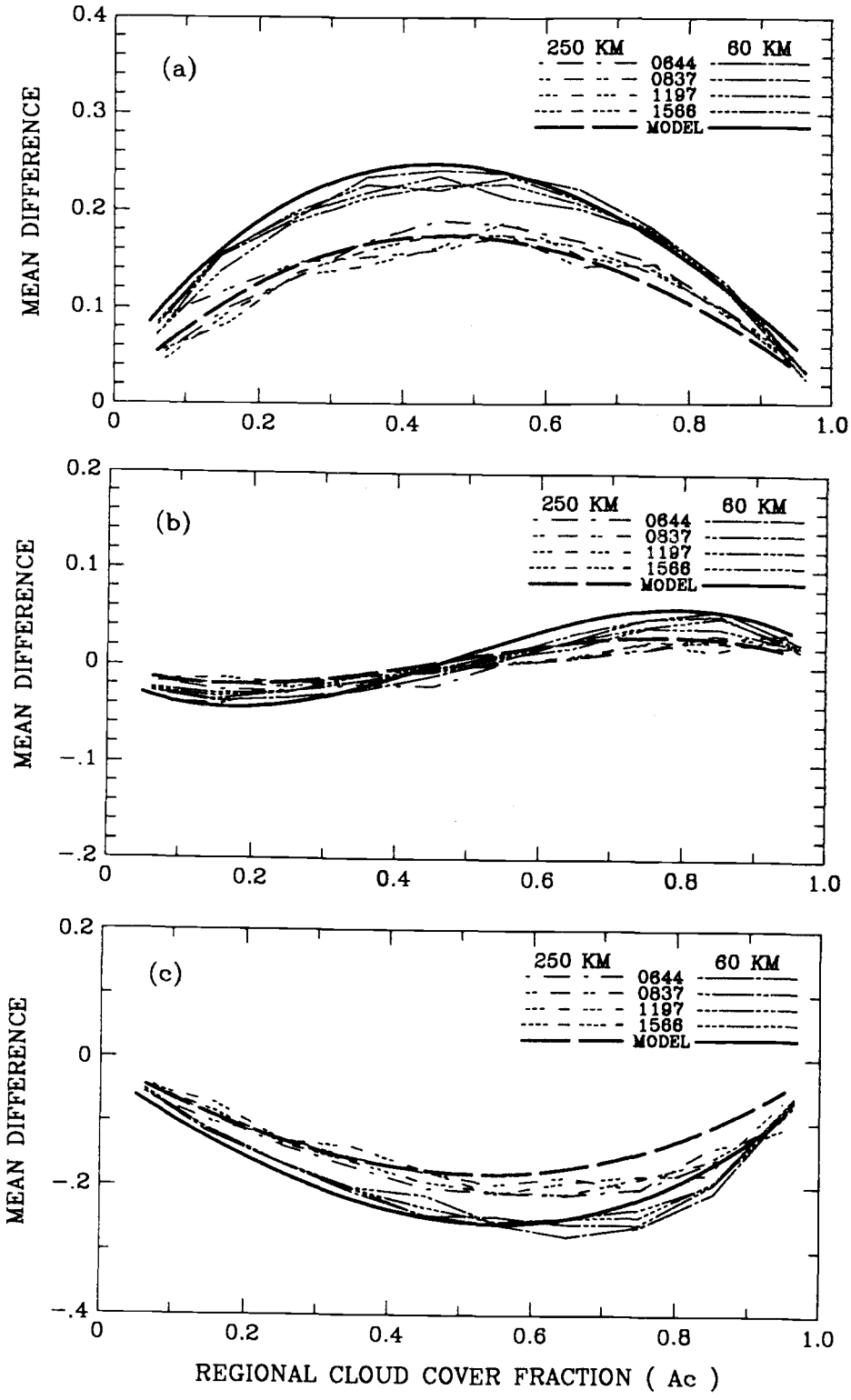

Figure 7.4 Mean differences for V-5 regions and that predicted by 2-parameter model. (a), (b), and (c) are respectively for the cloud-free threshold, midpoint threshold, and overcast threshold.

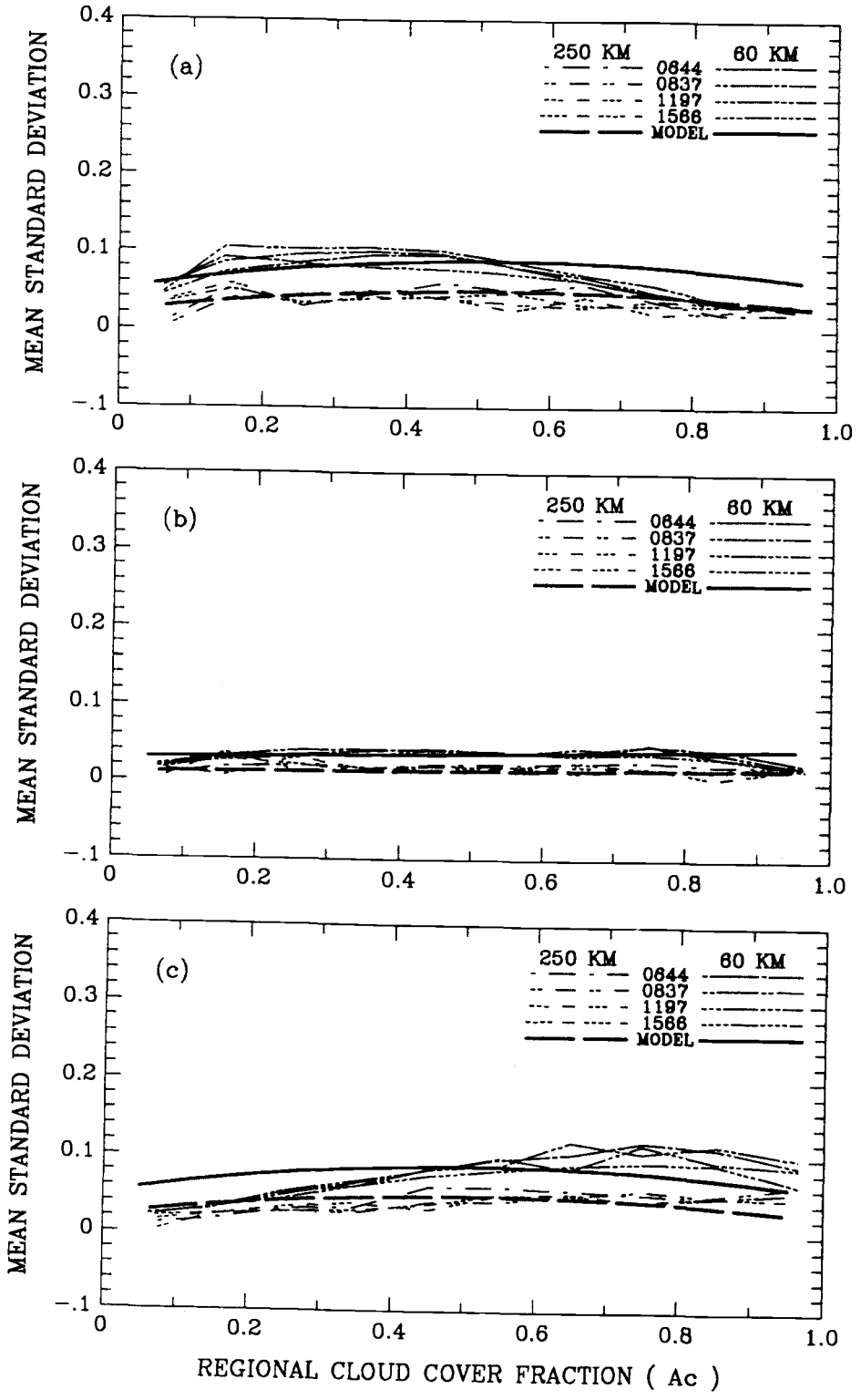

Figure 7.5 Standard deviations of mean differences in cloud cover for V-5 regions and that predicted by 2-parameter model. (a), (b), and (c) are respectively for the cloud-free threshold, midpoint threshold, and overcast threshold.

8. Conclusion and Discussion

The fractional cloud cover obtained using threshold methods was compared to that derived using the spatial coherence method for both (250 km)^2 and (60 km)^2 regions. The (250 km)^2 and (60 km)^2 regions used in this study contained single-layered systems for which the spatial coherence retrievals were judged to be good enough to serve as "truth" data. As shown in the previous sections, errors in cloud cover obtained with threshold methods are found to be large (overestimate 10–20% for (250 km)^2 scale and overestimate 15–25% for (60 km)^2 scale with an application of a conventional cloud-free threshold). The error approaches zero when the region is extensively cloud-free or extensively cloud-covered. The error also appears to be roughly symmetric with respect to the regional cloud-cover fraction. The maximum error occurs for regional cloud cover fractions of 0.5 and minimum errors occur for regional cloud cover fractions of 0.0 and 1.0. Threshold method derived cloud cover will generally be biased and will thus lead to biases in derived cloud radiative properties.

Threshold errors are caused by partially cloud-covered pixels. The errors are predictable if the frequency distribution of fractional cloud cover for partially covered pixels is known. Approximately 50% of the pixels appear to contain broken clouds. However, the time (several days) and space (tens of 60–250 km scale regions) averaged frequency distribution of pixel-scale cloud cover appears to be very stable. Furthermore, the averaged distribution of the partially covered pixels appears to be invariant from one V-5 region to the next. As a consequence, the mean threshold error and associated RMS are readily predicted.

In estimating errors due to threshold methods, several features of the pixel-scale distribution of fractional cloud cover were discovered. First, the distribution of partially covered pixels is a function of the regional-scale cloud cover. When a region has small cloud cover, the partially covered pixels included in the region also generally

contain small cloud cover. When a region has large cloud cover, the partially covered pixels included in the region also generally contain large cloud cover.

Second, the pixel-scale distribution appears to depend on the size of the region, such as $(60\ km)^2$ or $(250\ km)^2$. The reason that the distribution has a dependence on the size of the region is because of the different ways that clouds populate different sizes of regions. Small regions will have relatively few degrees of freedom in the distribution of pixel-scale cloud cover to achieve a particular regional coverage. For instance, a region of pixel-scale size will have only one way that it can achieve a particular cloud cover. A region of two pixel-scale size will have greater freedom to achieve a particular cloud cover and need not contain partially covered pixels to achieve 50% cloud cover. Large regions will have even more degrees of freedom and in this way, the pixel-scale distribution of fractional cloud cover becomes linked to the regional scale cloud cover.

Third, the pixel-scale distribution of fractional cloud cover and its dependence on regional-scale cloud cover seems appear to be universal. The same dependence is found in different parts of the earth. If this universality exists, then it allows the use of a simple distribution to represent the distribution of pixel-scale cloud cover for a region of particular size. In its simplest form, two theoretical models, a 1–parameter uniform distribution and a 2–parameter piecewise uniform distribution, are presented for estimating threshold errors.

In the 1–parameter model, the idealized distribution is obtained by assuming that partially covered pixels populate a uniform frequency distribution. In the 2–parameter model, the idealized distribution is obtained by assuming that partially covered pixels with fractional cloud cover less than 0.5 populate one uniform frequency distribution and those with fractional cloud cover greater than 0.5 populate another uniform frequency distribution. These models perform rather well in estimating the differences between cloud cover obtained by the spatial coherence method and those derived by threshold methods.

In this study, the spatial coherence method is assumed to provide realistic values of fractional cloud cover for single-layered systems. The differences between cloud cover obtained using the spatial coherence method and those derived using threshold methods are interpreted as threshold errors. However, the spatial coherence retrievals may be incorrect, e.g., clouds are not completely opaque at 11μm. Nevertheless, the simple models derived here seem plausible. It seems not unreasonable to assume that over large space and time scales, as used here, the partially covered pixels randomly populate a uniform distribution. Furthermore, it is assuring from a climate modeling point of view that the distribution of pixel-scale cloud-cover fraction might reflect the regional-scale cloud-cover fraction. For the large time and space scales used here, the connection between pixel-scale and regional-scale cloud-cover fractions may imply that the cloud-cover fraction at both scales is on average governed by large-scale processes. So, even though the spatial coherence results may not be worthy of the designation as a "truth" data set, the simple models for the pixel-scale distribution of fractional cloud cover may, nevertheless, provide useful tools for estimating errors in the fractional cloud cover obtained with threshold methods. In future work these simple models will be used to interpret the results of comparisons between the ISCCP derived and spatial coherence derived cloud properties.

Bibliography

Brost, R. A., D. H. Lenschow and J. C. Wyngaard, 1982a: Marine stratocumulus layers. Part I: Mean conditions. *J. Atmos. Sci.*, **39**, 800–817.

Brost, R. A., J. C. Wyngaard and D. H. Lenschow, 1982b: Marine stratocumulus layers. Part II: Turbulence budgets. *J. Atmos. Sci.*, **39**, 818–836.

Cahalan R. F., D. A. Short and G. R. North, 1982: Cloud fluctuation statistics, *Mon. Wea. Rev.*, **110**, 26–43.

Coakley, J. A., Jr. and F. P. Bretherton, 1982: Cloud cover from high-resolution scanner data: Detecting and allowing for partially filled fields of view. *J. Geophs. Res.*, **87**, 4917–4932.

Coakley, J. A., Jr., 1983: Properties of multi-layered cloud systems from satellite imagery. *J. Geophys. Res.*, **87**, 4917–4932.

Coakley, J. A., Jr. and D. G. Baldwin, 1984: Towards the objective analysis of clouds from satellite imagery data, *J. Climate and Appl. Meteor.*, **23**, 1065–1099.

Coakley, J. A., Jr., 1986: Effects of sensor spatial resolution on cloud properties retrieved from imagery data. *Extended Abstracts, Sixth Conference on Atmospheric Radiation, American Meteorological Society,* pp. 171–172.

Coakley, J. A., Jr., 1987: A dynamic threshold method for obtaining cloud cover from satellite imagery data, *J. Geophys. Res.*, **92**, 3985–3990.

Coakley, J. A., Jr. and T. Kobayashi, 1989: Broken cloud biases in albedo and surface insolation derived from satellite imagery data. *J. Climate,* **2**, 721–730.

Coakley, J. A., Jr., 1991: Reflectivities of uniform and broken layered clouds, *Tellus* (in press).

Kobayashi, T., 1988: Parameterization of reflectivity for broken cloud fields *J. Atmos. Sci.*, **45**, 3034–3045.

Minnis, P. and E. F. Harrison, 1984: Diurnal variability of regional cloud and clear-sky radiative parameters derived from GOES data. Parts I-III., *J. Climate and Appl. Meteor.*, **23**, 993–1051.

Minnis, P. and B. A. Wielicki, 1988: Comparison of cloud amounts derived using GOES and Landsat data, *J. Geophs. Res.*, **93**, 9385–9403.

Molnar, G., and J. A. Coakley, Jr., 1985: The retrieval of cloud cover from satellite imagery data: A statistical approach. *J. Geophs. Res.*, **90**, 12960–12970.

Ramanathan, V. and J. A. Coakley, Jr., 1979: Climate modeling through radiative-convective models, *J. Atmos. Sci.*, **24**, 241–259.

Ramanathan, V., R. D. Cess, E. F. Harrison, P. Minnis, B. R. Barkstrom, E. Ahmad, D. Hartmann, 1989: Cloud radiative forcing and climate: Results from the Earth Radiation Budget Experiment, *Science*, **243**, 57–63.

Rossow, W. B., F. Mosher, E. Kinsella, A. Arking, M. Desbois, E. Harrison, P. Minnis, E. Ruprecht, G. Seze, C. Simmer, and E. Smith, 1985: ISCCP cloud algorithm intercomparison, *J. Climate and Appl. Meteor.*, **24**, 877–903.

Rossow, W. B., L. C. Garder, and A. A. Lacis, 1989: Global, seasonal cloud variations from satellite radiance measurements, Part I: Sensitivity analysis, *J. Climate*, **2**, 419–458.

Schiffer R. A. and W. B. Rossow, 1983: The International Satellite Cloud Climatology Project: The first project of the World Climate Research Programme. *Bull, Amer. Meteor. Soc.*, **64**, 779–784.

Schmetz, J., 1984: On the parameterization of the radiative properties of broken clouds. *Tellus*, **36**A, 417–432.

Shenk, W. E., and V. V. Salomonson, 1972: A simulation study exploring the effects of sensor spatial resolution on estimates of cloud cover from satellites, *J. Appl. Meteor.*, **11**, 214–220.

Slingo, A., S. Nicholls and J. Schmetz, 1982: Aircraft observations of marine stratocumulus during JASIN. *Quart. J. Roy. Meteor. Soc.*, **108**, 833–856.

Wakefield, J. S., and W. H. Schubert, 1976: Design and execution of the marine stratocumulus experiment. *Atmos. Sci. Pap. No. 256, Colorado State University*, pp. 74.

Welch, R. M., B. A. Wielicki, 1984: Stratocumulus cloud field reflected fluxes: The effect of cloud shape. *J. Atmos. Sci.*, **41**, 3085–3103.

Wielicki, B. A., P. Minnis and L. Parker, 1986: The effect of spatial resolution on satellite derived cloud cover. *Extended Abstracts, Sixth Conference on Atmospheric Radiation, American Meteorological Society*, pp. 85–89.

Wielicki, B. A. and J.A. Coakley, Jr., 1981: Cloud retrieval using infrared sounder data: Error analysis. *J. Appl. Meteor.*, **20**, 157–169.

Wielicki, B. A. and R. M. Welch, 1986: Cumulus cloud field properties derived using Landsat digital data, *J. Climate and Appl. Meteor.*, **25**, 261–276.